J. Fluid Mech. (2012), *vol.* 695, *pp.* 405–438. © Cambridge University Press 2012
doi:10.1017/jfm.2012.29

High-enthalpy flow over a rearward-facing step – a computational study

N. R. Deepak†, S. L. Gai and A. J. Neely

School of Engineering & Information Technology, University of New South Wales, Australian Defence Force Academy, Canberra ACT 2600, Australia

(Received 9 May 2011; revised 21 November 2011; accepted 11 January 2012; first published online 20 February 2012)

Hypersonic, high-enthalpy flow over a rearward-facing step has been numerically investigated using computational fluid dynamics (CFD). Two conditions relevant to suborbital and superorbital flow with total specific enthalpies of 26 and 50 MJ kg^{-1}, are considered. The Mach number and unit Reynolds number per metre were 7.6, 11.0 and 1.82×10^6, 6.23×10^5 respectively. The Reynolds number based on the step height was correspondingly 3.64×10^3 and 12.5×10^2. The computations were carried out assuming the flow to be laminar throughout and the real gas effects such as thermal and chemical non-equilibrium are studied using Park's two-temperature model with finite-rate chemistry and Gupta's finite-rate chemistry models. In the close vicinity of the step, detailed quantification of flow features is emphasised. In particular, the presence of the Goldstein singularity at the lip and separation on the face of the step have been elucidated. Within the separated region and downstream of reattachment, the influence of real gas effects has been identified and shown to be negligible. The numerical results are compared with the available experimental data of surface heat flux downstream of the step and reasonable agreement is shown up to 30 step heights downstream.

Key words: boundary layer separation, gas dynamics, shock waves

1. Introduction

Ever since the design and development of intercontinental ballistic missiles during the 1950s and early 1960s, there has been a growing interest in hypersonic systems including manned and unmanned planetary missions and reusable transportation and space access systems such as the Space Shuttle orbiter. These vehicles travel typically at 7–10 km s^{-1}, thus covering both suborbital and superorbital velocities and high flight enthalpies, of the order of 20–50 MJ kg^{-1}. The extreme environment experienced by hypersonic vehicles during flight will always present an engineering and operational challenge as evidenced by the tragic loss of Space Shuttle Columbia in 2003 caused by excessive heating during atmospheric re-entry (Bertin & Cummings 2006) as a result of impact damage to the wing leading edge during launch. From an engineering view point, the aerothermodynamic conditions experienced with these high-enthalpy hypersonic flows need to be well understood for the design of efficient and reliable space vehicles. Some consequences of poor understanding of

† Email address for correspondence: deepak.narayan@gmail.com

https://doi.org/10.1017/jfm.2012.29 Published online by Cambridge University Press

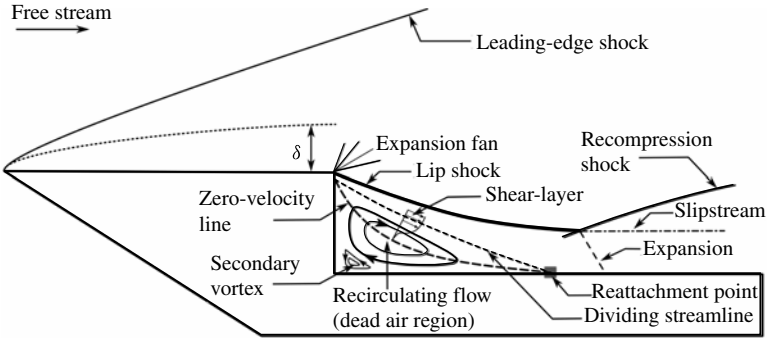


FIGURE 1. Schematic representation of flow features over a rearward-facing step.

aerothermodynamic phenomena include the ineffectiveness of the Space Shuttle flaps and tail protection system damage in the Gemini capsule due to inviscid/viscous interaction (Bertin & Cummings 2003). More catastrophic failures have included the shock/shock interaction on the X-15 that damaged the ventral fin during its Mach 6.7 test flight.

An important phenomenon that is often present in such hypersonic flights is the flow separation. This occurs due to the interaction of external and/or internal flows with various geometric design features, leading to adverse pressure gradients and consequent intense localised heating, thus changing the characteristics of the flow over the vehicle. Typical examples where flow separation occurs are behind blunt bodies, the vicinity of surface discontinuities such as steps and gaps, and deflection of control surfaces giving rise to shock wave/boundary layer interaction. The phenomenon of flow separation at high speeds therefore has received considerable attention over the past few decades due to its significance in the design of space vehicles. Although high-speed flow separation has been extensively investigated which has increased our knowledge considerably, large gaps still remain in our understanding of the aerothermodynamics of flow separation.

Flow separation can be effectively studied with simple configurations, representing a number of generic regions of separated flow on a space vehicle. These could range from flow over steps, forward facing or rearward facing, to compression corners and shock impingement on flat plates, etc. In the present investigation, a rearward-facing step is considered to examine flow separation. Figure 1 illustrates flow features over a two-dimensional rearward-facing step. A boundary layer (δ) develops as a consequence of flow over the flat plate upstream of the step, with the formation of a leading-edge shock wave. As the flow approaches the lip of the step, an expansion fan emerges through which the flow undergoes a strong expansion. In the vicinity of the top corner of the step, the boundary layer separates forming a free shear layer. The over-expansion of the flow at the corner is followed by a recompression to the base pressure through a lip shock. Due to strong over-expansion at the sharp corner, and because of viscous effects, the boundary layer separates at a finite distance from the corner and over the face of the step. The separated shear layer reattaches onto the plate some distance downstream. In this region, the compression waves coalesce to form a recompression or reattachment shock wave. As a result, the flow passing through it is aligned parallel to the plate surface. This region is termed the neck region due to the thinning of the shear layer before again growing downstream. A dividing streamline originates between separation and reattachment. For a two-dimensional flow,

https://doi.org/10.1017/jfm.2012.29 Published online by Cambridge University Press

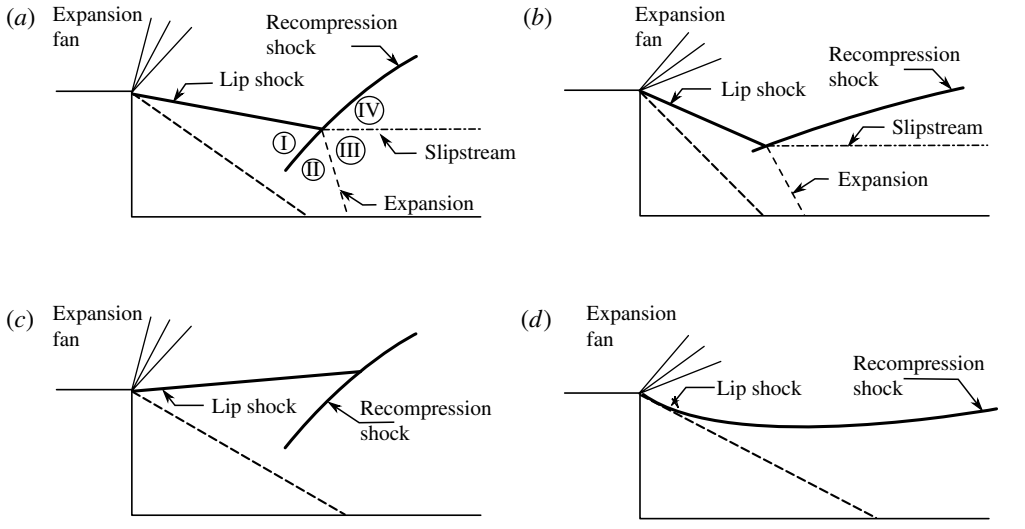


FIGURE 2. Influence of Mach and Reynolds number on lip–recompression shocks: (*a*) low Mach number, high Reynolds number; (*b*) high Mach number, high Reynolds number; (*c*) low Mach number, low Reynolds number; (*d*) high Mach number, low Reynolds number.

some of the flow gets trapped to form a recirculation region and this trapped region is often referred to as *dead air region* since there is no exchange of mass in and out of this region. Within the separated flow region, the zero velocity line delineates the flow in the forward and the reverse directions. Based on the free-stream Mach and Reynolds numbers the lip and the recompression shock orientation changes which results in the coalescence of the two shocks with the emergence of a slipstream and a weak expansion wave. A more detailed discussion on this is provided in the following paragraph. Depending upon the Reynolds number, a secondary vortex may form at the bottom corner between the face and the plate that has a counterclockwise direction.

It is well-known that the interaction of lip and recompression shocks is highly dependent on the Mach and the Reynolds number (Hama 1968). In figure 2, different possibilities are schematically shown as experimentally confirmed by Hama. We note that at low Mach and high Reynolds numbers, both the lip and the recompression shock can be clearly identified. At sufficiently high Reynolds number, a slipstream parallel to the shear layer emerges from the location where the lip and recompression shocks coalesce and is followed by a weak expansion wave. Due to this shock–shock interaction and subsequent expansion, the flow in the near wake undergoes series of changes, eventually affecting surface parameters like pressure and heat flux. This can be best explained through figure 2(*a*), where the shear layer post-separation is initially compressed by a lip shock (region I) and the pressure here is approximately equal to the base pressure (Hama 1968). The same flow is further compressed through the recompression shock (region II), while the flow in region IV, only being compressed by recompression shock has lower pressure than in region II and thefore is balanced by an expansion wave. This expansion wave hitting the plate causes the pressure and heat flux to reduce during the recovery process. Regions III and IV are separated by a slipstream. Referring to figure 2(*b*), as the Mach number increases, the lip and recompression shocks tend to merge to form one single shock structure which is

https://doi.org/10.1017/jfm.2012.29 Published online by Cambridge University Press

particularly noticeable at low Reynolds number where the flow is fully laminar. In this case the emergence of the slipstream may not be prominently visible as in the case of higher Reynolds number. Also to note is the orientation of the lip shock with respect to the formation of the shear layer. At low Mach and higher Reynolds numbers (figure 2*a*), the lip shock orientation appears to be quite shallow and extends out rather quickly from the shear layer. At high Mach number and low Reynolds number (figure 2*d*), the lip shock orientation is quite steep and is completely embedded within the thick separated shear layer. In addition, a part of the recompression shock that coalesceses with the lip shock is also embedded in the shear layer. More discussion regarding these in conjunction with the present results will be presented in § 6.

Despite the rearward-facing step being a convenient configuration to examine, there have been very few studies of it. Numerical data are particularly sparse. Roache & Mueller (1968), Allen & Cheng (1970), Ross & Cheng (1971), Corda (1982), Priolo (1983), Kuruvila & Anderson (1985) and Khan & Hoffmann (2010) are some of the studies in supersonic flow. In hypersonic flow for example, data from Gai & Milthorpe (1995), Borovoi, Skuratov & Yegorov (1998), Grotowsky & Ballmann (2000), Hayne *et al.* (2002) and Leite & Santos (2009) may be mentioned. These studies, however, have been carried out at low enthalpies or under a perfect gas flow assumption. Experimentally, the flow behind a rearward-facing step has been investigated by Rom & Seginer (1964), Baker & Martin (1966), Scherberg & Smith (1967) and Sandford & Ginoux (1968) in supersonic flow. Wada & Inoue (1973) were, perhaps, the first to investigate this flow at hypersonic conditions. These experiments, however, were largely under quite low-enthalpy conditions where real gas effects would not be significant. Experimental studies by Gai *et al.* (1989) and Gai (1992) were the first to investigate high-enthalpy flow behind the step up to 19 MJ kg^{-1} with partially dissociated air in a free piston shock tunnel. Subsequently Gai *et al.* (2001) examined superorbital flow of air at specific enthalpies of 30 and 47 MJ kg^{-1} in an expansion tube facility, X2, at the University of Queensland. More recently, Hayne (2004) investigated high-enthalpy flow of air at specific enthalpies of 26 and 50 MJ kg^{-1} more extensively in the same X2 expansion tube facility. These have been the highest range of enthalpies studied experimentally so far.

The current study therefore aims to complement these high-enthalpy experiments with numerical investigation with particular emphasis on the aerothermodynamics of separated flows and thermo-chemical non-equilibrium effects using different thermo-chemical models. For the flows considered here, real gas effects are inherently present and thus the significance of these in the regions of flow separation is an important aspect of the study. This is because of the complicated nature of the flow field and several phenomena occurring simultaneously along with real gas physics. This necessitates a thorough validation of computational codes and physico-chemical models used and a comparison with the available experimental data, however, sparse. Only laminar flow calculations have been performed in view of the low Reynolds numbers encountered. To the authors' knowledge, no numerical data exist in the enthalpy range considered here.

2. Geometric configuration and flow conditions

The geometry consists of an upstream forebody flat plate of length (L) 48.4 mm with a sharp leading edge and a step of height (h) of 2 mm. The ratio of step

https://doi.org/10.1017/jfm.2012.29 Published online by Cambridge University Press

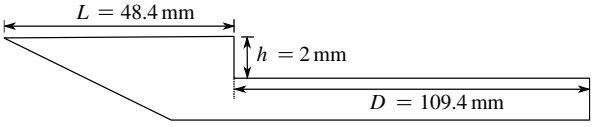


FIGURE 3. Rearward-facing step geometry.

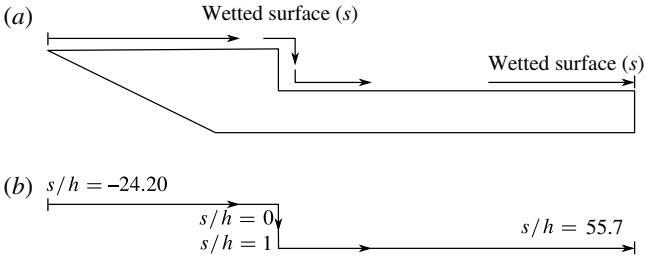


FIGURE 4. Schematic of coordinate system for the step: (*a*) details of the wetted surface; (*b*) coordinate system for the step.

height (h) to length (L) is thus 0.041. Downstream of the step, a flat plate of length (D) extends the model by 109.4 mm. This geometric configuration remains identical for the two flow conditions investigated here. A schematic representation of the geometry is shown in figure 3.

A basic coordinate system, which was originally introduced by Hillier in Hayne *et al.* (2002) to present the numerical results of flow over the step, is used to present all the subsequent data and results. In this system, the forebody, step and downstream plate surfaces are expressed in terms of a continuous wetted surface (s). They are then normalised by h and referenced such that $s/h = 0$ represents the top corner of the step and $s/h = 1$, its bottom corner. A schematic of the coordinate system is shown in figure 4. Based on the geometric dimensions given in figure 3, the forebody leading edge attains values of $s/h = -24.20$, and $s/h = 55.7$ for the trailing edge of the downstream plate.

The experimental investigation using this configuration was conducted in the University of Queensland X2 expansion tube facility with air as the test gas at total specific enthalpies of 26 and 50 MJ kg^{-1} respectively (Hayne 2004). As can be seen from figure 3, a step height of 2 mm was chosen in the experiments. This is because the test times available in the X2 expansion tube are of the order of 90 μs or less depending on the enthalpy. Due to such short durations, the main concern is to ensure that a steady flow over the flat plate and subsequent steady separated flow behind the step can be achieved. It is also well-known that the establishment time varies with respect to the scale of the separated region and with larger step or base height the flow establishment time increases (Holden 1971). Previous experimental studies on rearward-facing steps in short duration facilities have been conducted with small step heights to facilitate the flow establishment criterion (Rom & Seginer 1964; Gai *et al.* 1989, 2001). Since a direct comparison of the experimental data obtained by Hayne (2004) is made in this study, an identical geometric configuration of 2 mm step height is subjected to computational investigation at the same flow conditions. In view

https://doi.org/10.1017/jfm.2012.29 Published online by Cambridge University Press

Flow parameter	Suborbital condition	Superorbital condition
Test gas	Air	Air
Total specific enthalpy, H_o (MJ kg^{-1})	26.0	50.0
Pressure, p_∞ (kPa)	10.43	1.58
Temperature T_∞ (K)	1813	1475
Density ρ_∞ (kg m^{-3})	17.32 $\times 10^{-3}$	3.676 $\times 10^{-3}$
Velocity, u_∞ (m s^{-1})	6872	9652
Mach number, M_∞	7.6	11.0
Specific heat ratio, γ_∞	1.34	1.41
Reynolds number, Re_∞ (m^{-1})	1.82 $\times 10^6$	6.23 $\times 10^5$
Mass fraction		
X_{N_2}	0.770	0.665
X_N	0.000	0.115
X_{O_2}	0.050	0.000
X_O	0.160	0.220
X_{NO}	0.020	0.000

TABLE 1. X2 flow conditions.

of this small step height, thin film gauges were predominantly mounted downstream of the step.

The flow past a rearward-facing step at suborbital and superorbital conditions is simulated under the assumption of two-dimensional flow. Experimental investigations of hypervelocity flows over steps have shown them to be at least nominally two-dimensional, see for example, Rom & Seginer (1964) and Wada & Inoue (1973) and Gai *et al.* (1989). More recently, Hayne *et al.* (2004) conducted experiments on the flow over a rearward-facing step at suborbital and superorbital speeds in an expansion tube in which he established that the flow was nominally two-dimensional over at least 2/3 of the span. Since one of the aims of the present investigation is to complement the experimental data of Hayne (2004), all CFD simulations are performed assuming two-dimensional flow.

The experiments by Hayne (2004) were carried out at enthalpies corresponding to both suborbital and superorbital speeds. Due to the presence of nonlinear effects in the expansion tube, Hayne performed a Lagrangian one-dimensional inviscid computational simulation (L1D) of the expansion tube flow to determine the nominal flow conditions. To account for the effects of chemistry, a finite-rate module with 5 species and 17 reactions for air was modelled by Hayne (2004). In addition, Hayne also included a full Navier–Stokes simulation of the expansion tube flow to incorporate viscous effects. Table 1 summarises the flow conditions used for the present simulations. It should be noted that these flow conditions do not reflect any particular flight trajectory, but cover the specific total enthalpy typically experienced during orbital re-entry. Hence, due to the nature of the operation of an expansion tube, the test gas temperature is considerably raised due to the propagation of the primary shock wave and thereby giving rise to high free-stream temperatures. The gas species concentrations given in table 1 are evaluated based on the finite-rate chemistry (Hayne 2004). For the computational simulation of the thermal non-equilibrium condition, the vibrational temperature (T_v) is assumed to be in equilibrium with the translational temperature (T_t).

https://doi.org/10.1017/jfm.2012.29 Published online by Cambridge University Press

3. Computational approach

3.1. *Computational codes and models*

The computations used two compressible multi block Navier–Stokes solvers, MB-CNS-2 (Jacobs 1991, 1996) and Eilmer-3 (Jacobs & Gollan 2010; Jacobs *et al.* 2010). One of the primary reasons for using Eilmer-3 in this investigation is its capability to study the thermo-chemical non-equilibrium behaviour of air utilising the two-temperature kinetic model of Park (1993). A brief description of the modelling approach used by these two codes is presented here, but a more comprehensive account is given in Deepak (2010). These codes solve time-accurate Navier–Stokes equations in two dimensions using the cell-centred finite-volume approach.

MB-CNS-2 and Eilmer-3 utilise the van Albada, Leer & Roberts (1982) limiter and the monotone upstream-centred schemes for conservation laws (MUSCL) (Leer 1979; Anderson & Thomas 1986) reconstruction scheme to obtain a second-order upwind interpolation. While the inviscid fluxes are calculated at the cell interfaces using advection upwind splitting method combining difference and vector splitting (AUSMDV) (Wada & Liou 1994), the viscous fluxes are calculated using the averaged values of the viscous stresses at the cell vertices. The time integral is numerically iterated using the predictor–corrector scheme and the time advancement is based on the time-splitting or operator-splitting technique (Gollan 2008; Jacobs *et al.* 2010). Explicit time integration is used and numerical stability is maintained via the Courant–Friedrich–Lewy (CFL) criterion, and the stability is achieved in the range $0 \leqslant \mathrm{CFL} \leqslant 0.5$. Hence, all the CFD computations are performed with a CFL value of 0.5.

The simulations were performed both under the assumption of perfect gas as well as considering chemical and thermal non-equilibrium effects. For the CFD calculations involving a perfect gas assumption, the test gas is assumed to behave as a single species while the thermodynamic behaviour was calorically perfect with a constant ratio of specific heats (γ). Viscosity (μ) was modelled using the Sutherland formulation and thermal conductivity (k) was calculated using $k = \mu C_p/Pr$, where C_p is specific heat at constant pressure and Prandtl number (Pr) is assumed to be 0.72. For simulations involving chemical and thermal non-equilibrium, the test gas was modelled as five species and the mass fractions relevant to the conditions given in table 1 are used. Finite-rate-chemistry simulations were performed using two well-known reaction schemes in order to model the chemical non-equilibrium effects of high temperature air. In the first, where only chemical non-equilibrium is considered, the Gupta *et al.* (1990) kinetic scheme is used which is described by a 20 set reaction model for high-temperature air, up to 30 000 K, represented by 11 species aimed at modelling dissociation–recombination, exchange and ionisation reactions. In the current investigation, only five neutral species (N_2, O_2, NO, O and N) that contribute towards dissociation–recombination and exchange reactions are considered with any effects of ionisation being ignored. However, since the non-equilibrium flow over a slender body is investigated here, the dissociated species may not be subjected to ionisation, unlike in the forebody region of a blunt body. Therefore, modelling with five neutral species should be a reasonable assumption.

For simulations involving chemical and thermal non-equilibrium, the Park (1993) scheme described by 23 reactions for high-temperature air represented by 11 species is used. However, a five neutral species implementation is adapted here so as to be consistent with the previous choice of species from the Gupta *et al.* (1990) scheme. This scheme has received particular attention in recent years, due to its capability

https://doi.org/10.1017/jfm.2012.29 Published online by Cambridge University Press

of modelling two temperatures at an additional cost of solving only a single partial differential equation for the total vibrational energy (Ait-Ali-Yahia 1996). As this model is computationally less expensive than a more complicated multi-temperature model, it is widely implemented in CFD codes (Ait-Ali-Yahia 1996).

For the set of chemical kinetic schemes, the reaction rate coefficients were calculated based on the generalised Arrhenius form. The finite-rate chemical reactions were modelled as a set of ordinary differential equations using a quasi-steady-state method, alpha-QSS (Mott 1999). Another important criterion to be considered here is to ensure that the mass due to a chemical reaction is conserved at every chemical time step. This is achieved by scaling the mass fraction of the participating species at the end of every time step such that the mass due to chemistry is conserved (Gollan 2008). This approach is called renormalisation and is believed to be more precise than the common approach of solving $(N-1)$ species for conservation (Gollan 2008). The thermodynamic behaviour of these reactive species is based on the mixture of thermally perfect gases. Therefore, the species have perfect collisional behaviour and the values of specific heats at constant pressure (C_p) and constant volume (C_v) are functions only of the temperature. The values of C_p are modelled individually for every species using a polynomial curve fit outlined by NASA Glenn computer code program, CEA (Chemical Equilibrium with Applications) (Gordon & McBride 1994; McBride & Gordon 1996) which is valid up to 20 000 K. The modelling of transport properties is again based on the CEA approach in which the individual species properties are first modelled from the CEA polynomial curve fits and then the Wilke (1950) mixing rule is used to compute the viscosity and thermal conductivity of the mixture.

The thermal non-equilibrium effects were based on the two-temperature model of Park (1993). Here, a translational–rotational temperature (T_t) and a vibrational–electronic temperature (T_v) are modelled. The energy exchange between the vibrational and translational modes is modelled based on the Landau–Teller equation and the vibrational relaxation time is calculated based on the Millikan & White (1963) empirical correlation, which is of the form shown in Park (1993). The vibrational energy is calculated based on the harmonic oscillator model which provides an average vibrational energy in a Boltzmann distribution; and the value of C_v is estimated based on the harmonic oscillator model and C_p is estimated using $C_p = C_v + R$, R being a specific gas constant. It should be pointed out that the Landau–Teller model may fail to predict the actual de-excitation processes occurring in expanding flows (Ruffin & Park 1993; Paciorri, Sabetta & Favini 1998). Therefore, some caution has to be exercised when calculating relaxation time based on the Landau–Teller model. The transport properties in this case are modelled using the Gupta *et al.* (1990) mixing rule.

3.2. *Grid independence study*

A complete description of the grid independence study carried out for this configuration is reported in Deepak, Gai & Neely (2010*a*,*b*) and Deepak (2010). Here only a brief account is provided along with details of the grid convergence index (GCI) (Roache 1997) used to determine the relative error between the grids used.

The computational domain considered here is shown in figure 5 with multiple blocks which are precisely interconnected node-to-node. Although not very apparent in the figure, the far upstream block has a free-slip wall. This ensures that the boundary layer growth from the sharp leading edge is not affected and the inflow condition is well-posed. It should be noted here that the experimental model has

https://doi.org/10.1017/jfm.2012.29 Published online by Cambridge University Press

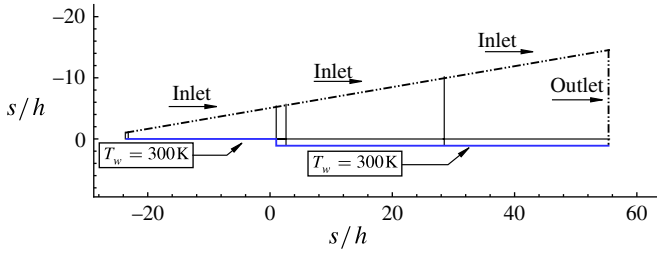


FIGURE 5. (Colour online available at journals.cambridge.org/flm) Computational domain and boundary conditions.

a sharp leading edge with a bevel angle of 25° (Hayne 2004). However, for the purpose of computational modelling a zero-bluntness leading edge is assumed. The upstream flat plate, step and downstream plate are modelled as a cold wall with a fixed temperature of $T_w = 300$ K. This should be a valid assumption as during experiments, the rise in surface temperature is quite small even at high-enthalpy conditions due to the short test times. Various computational investigations (Deepak *et al.* 2010*a*,*b*; Park, Gai & Neely 2010) have also been carried out by modelling the wall temperature under similar assumptions. The top external boundaries are used to provide uniform supersonic inlets and the supersonic outlet is provided at the trailing edge of the downstream plate. As can be seen in figure 5, the computational domain extends from $s/h = -24$ (at the leading edge) up to 54 step heights from the step which covers the entire upstream and downstream region of the experimental model. In view of using time-accurate codes, certain assumptions have to be made which are noted. Primarily, an exact starting scenario of the expansion tube is not simulated here as this is beyond the scope of the present work. Thus, test-gas contamination from acceleration gas is neglected. Nevertheless, the initial conditions such as pressure, velocity and temperature are applied similarly to the conditions that are present in the test section at $t = 0$ s. These conditions are of course uniform and are initialised from every grid point in the computational domain, including at the solid boundaries. Secondly, the inflow boundary conditions are tailored to accommodate uniform free-stream properties along the oblique inlets of the computational domain (see figure 5). This does not account for any spatial flow non-uniformity that may be encountered and these assumptions may therefore differ from the actual start-up process.

The grid independence computations for both suborbital and superorbital flow were performed under the assumption of perfect gas. This can be justified on the following grounds. Firstly, in the perfect gas assumption, air is modelled as a single species, while for the real gas, air is generally treated as multiple species; the only difference is that the latter takes longer for grid convergence. Secondly, both these codes are based on explicit time integration and the stability is achieved via the CFL number and is fixed at CFL = 0.5. For the current grid converged solution, the smallest grid size (first cell from the wall) is 2×10^{-5} m and thus, the time step (Δt) will be of the order of 1×10^{-9} s, based on a free-stream velocity of 6700 m s^{-1} and a CFL value of 0.5. To attain a steady-state solution, which is approximately 160 μs for suborbital conditions (Deepak 2010), the total time steps required are $\sim 1 \times 10^6$. Therefore, even for a perfect gas analysis the computational time requirements for solving this many time steps would be enormously expensive, which has also been noted by Druguet, Candler & Nompelis (2005). Other researchers, such as Gnoffo (2001), Druguet, Ben-Dor & Zeitoun (2007) and Gollan (2008) have also adopted the strategy of using perfect gas

https://doi.org/10.1017/jfm.2012.29 Published online by Cambridge University Press

Grid	$i \times j$	Δ_w (μm)	Vicinity of step (VOS)
Grid-1	60 × 25	100	10 × 10
Grid-2	120 × 50	50	20 × 20
Grid-3	240 × 100	25	27 × 40
Grid-4	288 × 120	20	46 × 48
Grid-5	410 × 120	20	80 × 48
Grid-6	410 × 152	20	80 × 90

TABLE 2. Various grids used for the grid independence study.

Grid	Separation (s/h)	GCI_s	Reattachment (s/h)	GCI_r
Grid-1	0.126	4.80×10^{-2}	2.48	5.86×10^{-2}
Grid-2	0.090	1.50×10^{-2}	2.63	1.83×10^{-2}
Grid-3	0.074	6.66×10^{-3}	2.63	4.34×10^{-2}
Grid-4	0.075	2.84×10^{-3}	2.60	8.53×10^{-2}
Grid-5	0.075	0.00	2.59	6.55×10^{-3}
Grid-6	0.076	4.96×10^{-4}	2.59	0.00

TABLE 3. Separation and reattachment distance for various grids for suborbital flow.

model for grid independence studies. Consequently, this grid independence study was limited to the perfect gas assumption. It is, therefore, possible that while the effects associated with real gas effects may indicate some small quantitative shifts, they are likely not to result in any major qualitative change.

The initial grid (Grid-1) comprised $60i \times 25j$ cells with the first cell height from the wall being $\Delta_w = 100$ μm. A subsequent refinement of the grid was then performed with the cells in both the i and j directions being doubled and Δ_w reduced by a factor of 0.5. Details of each grid and its relevant Δ_w are shown in table 2. Over the forebody region, step face and plate past the step the grids are clustered using hyperbolic expansion and the first cell is at $\Delta_x = \Delta_y = \Delta_w$, where Δ_x and Δ_y are the first cell height in the x and y directions respectively. In figure 6, details of the grid are illustrated for Grid-5. Jackson, Hillier & Soltani (2001) and others (Papadopoulos *et al.* 1999; Bertin & Cummings 2006) consider the surface heat flux as one of the critical variables for determining grid independence since this is said to provide a sensitive test for CFD calculations. In the present investigation also, the surface heat flux is chosen for determining grid independence in addition to considering the skin friction coefficient.

Table 3 gives the non-dimensional separation and reattachment distances from $s/h = 0$ (top corner) for various grids. The grid convergence index (GCI), based on the generalised theory of the Richardson extrapolation (Roache 1997), is used to determine the relative error between the grids used. The index is generally considered to be the standard method for reporting grid uncertainty in numerical simulations involving CFD (Roache, Ghia & White 1986; AIAA 1994). In this technique, the variable of interest for finer and coarser grids is used to estimate the relative error between them (Roache 1997). In table 3, GCI_s and GCI_r are the relative errors obtained for the separation and reattachment locations respectively. It should be noted that the GCI_s between Grid-5 and Grid-6 is 4.96×10^{-4} and the corresponding GCI_r is 6.55×10^{-3}. For these grids, the reattachment locations are predicted to be $s/h = 2.59$,

https://doi.org/10.1017/jfm.2012.29 Published online by Cambridge University Press

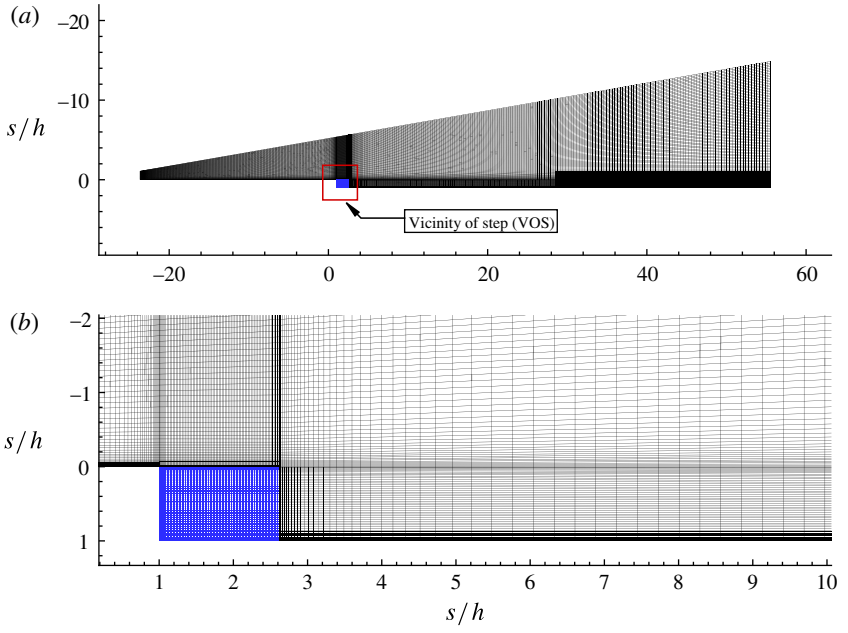


FIGURE 6. (Colour online) Distribution of grids for the rearward-facing step (Grid-5). (*a*) Representation of the grid in the computational domain; (*b*) details of the grid in vicinity of the step.

Grid	Separation (s/h)	GCI_s	Reattachment (s/h)	GCI_r
Grid-1	0.3539	8.125×10^{-2}	1.92802	8.092×10^{-2}
Grid-2	0.2929	2.539×10^{-2}	1.98872	2.529×10^{-2}
Grid-3	0.2839	3.771×10^{-3}	1.98219	2.721×10^{-3}
Grid-4	0.3023	5.238×10^{-2}	1.96583	4.646×10^{-2}
Grid-5	0.3023	0.00	1.96423	7.963×10^{-4}
Grid-6	0.3021	1.282×10^{-4}	1.96423	0.00

TABLE 4. Separation and reattachment distance for various grids for superorbital flow.

which is 1.59 step heights from the step face. This is in close agreement with the predictions made in Hayne *et al.* (2002) where the reattachment distance is given as 1.53 step heights. Experimentally it is estimated to be around 1.6 step heights based on holographic interferometric flow visualisation (Hayne *et al.* 2003). Also, from both the surface heat flux and skin friction coefficient comparative distributions given in Deepak *et al.* (2010*a*,*b*) and Deepak (2010), it would appear that solutions should be grid independent with Grid-5 and above. All further computations are therefore made using this grid.

The grid sensitivity in the case of superorbital flow is estimated using identical grids (Grid-1 to Grid-6) as in suborbital flow. Eilmer-3 code was used for this exercise. Sensitivity of heat flux and skin friction distributions in regions of separation and reattachment was similar to that of suborbital flow and is fully discussed in Deepak (2010). Table 4 presents the non-dimensional separation and reattachment distances

https://doi.org/10.1017/jfm.2012.29 Published online by Cambridge University Press

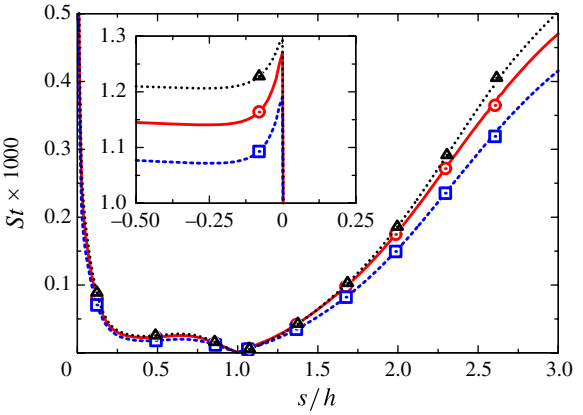


FIGURE 7. (Colour online) Stanton number distributions in the vicinity of the corner (inset) and between separation and reattachment in suborbital flow, $H_o = 26$ MJ kg^{-1}: $-\odot-$, perfect gas; $--\boxdot--$, chemical non-equilibrium; $--\triangle--$, chemical-thermal non-equilibrium.

from the top corner ($s/h = 0$) for different grids. The GCI is evaluated in a similar manner to that for suborbital flow. The GCI$_s$ for separation, between Grid-5 and Grid-6, is 1.282×10^{-4}; correspondingly, for reattachment GCI$_r = 7.963 \times 10^{-4}$. Based on GCI values presented in the table, it would appear that the solutions should be grid independent with Grid-5 and beyond. Hence all computations relevant to superorbital flow have also been carried out using Grid-5.

4. Results and discussion: suborbital flow

4.1. *The vicinity of the step*

Quantification of flow features in the vicinity of the top corner and in the separation/reattachment regions are considered by investigating the distributions of heat flux, skin friction and pressure. The non-dimensional heat flux (Stanton number, St), skin friction coefficient (c_f) and normalised pressure (p/p_∞) distributions are plotted along the upstream flat plate, close to the corner and then between separation and reattachment, and extending downstream, as per the step coordinate system defined in figure 4. Here, the top separation lip is at $s/h = 0$, and $s/h = 1$ is the bottom corner of the step, and $s/h \geqslant 1$ is the distance down the plate. Initially comparisons are made between perfect and real gas calculations and are subsequently compared with available experimental data downstream of the step.

The Stanton number distributions for the present computations are estimated from

$$St = \frac{q_w}{\rho_e u_e (h_r - h_w)} \tag{4.1}$$

where q_w is the surface heat flux estimated from $k(\partial T/\partial y)$, and h_r is the recovery enthalpy evaluated from

$$h_r = h_e + \sqrt{Pr}\,\frac{u_e^2}{2}. \tag{4.2}$$

In figure 7, the Stanton number distributions are presented in the regions of separation and reattachment for the perfect gas model, the chemical non-equilibrium model of Gupta *et al.* (1990) and the chemical plus thermal non-equilibrium model

https://doi.org/10.1017/jfm.2012.29 Published online by Cambridge University Press

of Park (1993) for a 26 MJ kg^{-1} flow condition (hereafter referred to as perfect gas, chemical non-equilibrium and chemical plus thermal non-equilibrium). The inset in figure 7 shows results over the forebody region extending up to the corner. We note that chemical plus thermal non-equilibrium calculation estimates the highest heat flux while chemical non-equilibrium calculation predicts the lowest. Very close upstream of the corner, all the three simulations show a steep rise as the corner is approached. Further elucidation of this particular phenomenon is given in the following paragraphs when discussing skin friction distributions.

The difference in Stanton number distributions is due to the inherent differences between the two codes (Deepak 2010). Although not presented here, the prediction from the perfect gas data obtained from Eilmer-3 is higher than from the corresponding real gas data so that both codes are internally self-consistent. Nevertheless, with further investigation, it was found that the increased heat flux noted with Eilmer-3 computation in comparison to MB-CN-2, particularly for perfect gas, was due to the relative increase in absolute temperatures within the boundary layer. This resulted in an increase in temperature gradients as well as thermal conductivity, eventually increasing the heat flux at the wall. This discrepancy is currently being investigated (P. Jacobs 2010, personal communication), although it has recently been pointed out by R.J. Gollan (2010, personal communication) that Eilmer-3 does not assume a constant Prandtl number, unlike MB-CNS-2 for perfect gas, which could lead to different estimations of thermal conductivity.

The variation in the thermal conductivity values is due to the following factors. Firstly, the values of thermal conductivity used to evaluate heat flux are taken from the cell-centre of the first cell adjacent to the wall. Therefore, the thermal conductivity becomes a function of cell-centred temperature. Secondly, the mixing rule for the transport properties is different in the two real gas models. Chemical non-equilibrium uses the Wilke (1950) rule, while chemical plus thermal non-equilibrium uses the Gupta–Yos (Gupta *et al.* 1990) rule. Hence, a small variation in species concentration over the wall changes the mixing properties and influences the thermal conductivity values, which in turn affects the heat flux. A similar state of affairs is also noted by Chen *et al.* (1993) for chemically reactive flows, where the surface heat flux was seen to vary with variations in thermal conductivity under non-catalytic wall conditions. This highlights the uncertainty that may arise in the estimation of transport properties close to the wall where the gas is composed of both neutral and dissociated species, even though the cell temperature is close to the wall temperature.

In figure 7 values beyond $s/h \geqslant 0$ represent distributions on the step face and between separation and reattachment over the plate. Small differences in the Stanton number values over the step face ($0 \leqslant s/h \leqslant 1$) can be seen as they gradually approach zero at the bottom corner. The trends for the these three data sets are consistent with those seen on the forebody. Over the plate surface between $1 \leqslant s/h \leqslant 3$, some differences are noted. The heat flux in all three cases monotonically increases from zero at the bottom corner with increasing distance downstream. Although, initially, within about a step height ($s/h \approx 2$), all the data are quite close, they start to deviate considerably from each other as the reattachment is approached at $s/h \approx 2.5$.

All the simulations show that while differences exist upstream and downstream of the corners, chemical and chemical plus thermal non-equilibrium effects do not severely affect the separated region and that the flow is frozen in the cold recirculation region. The differences in heat flux observed for different codes are considered to be mainly due to the choice of different thermodynamic and transport properties as well as some inherent differences between the codes themselves.

https://doi.org/10.1017/jfm.2012.29 Published online by Cambridge University Press

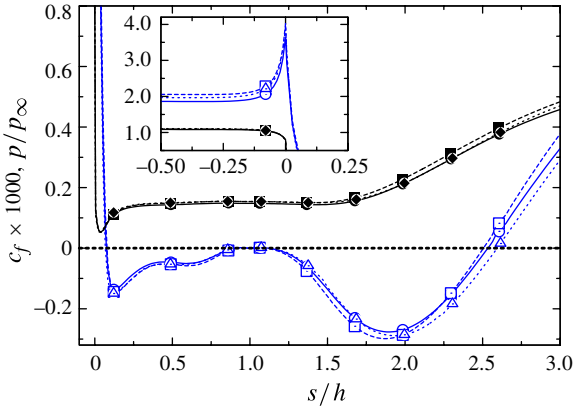


FIGURE 8. (Colour online) Skin friction coefficient and pressure distributions in the vicinity of the corner (insert) and between separation and reattachment in suborbital flow, $H_o = 26$ MJ kg^{-1}: ($c_f \times 1000$: $-\odot-$, perfect gas; $--\boxdot---$, chemical non-equilibrium; $\cdots\triangle\cdots$, chemical-thermal non-equilibrium); (p/p_∞: $-\bullet-$, perfect gas; $--\blacksquare---$, chemical non-equilibrium; $\cdots\blacklozenge\cdots$, chemical-thermal non-equilibrium).

In figure 8, the skin friction and pressure distributions in the regions of separation and reattachment are shown. Specifically, close to the lip of the step, the rise in skin friction as the corner is approached should be noted, as shown in the inset. This particular behaviour of skin friction (and Stanton number) as the corner discontinuity is approached from upstream is due to the *Goldstein singularity* (Goldstein 1946; Stewartson 1968; Hayne *et al.* 2002). Such asymptotic increases in skin friction and heat flux have also been noted by Grotowsky & Ballmann (2000) and Gorshkov & Lunev (2002) as well as Hollis & Perkins (1999). As can be seen in figure 8 where the distributions over the face ($0 \leqslant s/h \leqslant 1$) are shown, the skin friction following the peak at the corner falls and crosses zero at $s/h \approx 0.0759$. Thus separation occurs not at the corner ($s/h = 0$), but on the face of the step. This feature of separation around a sharp corner has been pointed out previously by Weinbaum (1966), Donaldson (1967), Hama (1968) and Jakubowski & Lewis (1974) and more recently, Grasso & Pettinelli (1995) and Gorshkov & Lunev (2002). It occurs because of strong over-expansion which turns the viscous flow around the corner followed by separation from the face of the step. Gorshkov & Lunev (2002) interestingly argue that the flow ejecting from the mixing zone and the flow arriving from the base can be dynamically compatible only when separation occurs over the face of the base.

After the flow separates, the skin friction reaches a minimum and gradually increases thereafter until it again reaches zero at $s/h = 1$. In general, the values of skin friction do not vary among the three simulations over the face of the step. After $s/h \geqslant 1$, the skin friction values decrease and attain negative values, then reach a minimum between $1.8 \leqslant s/h \leqslant 2.0$. They then gradually increase and cross the zero value where the flow reattaches. Separation and reattachment distances are presented in table 5 and some differences in separation and reattachment locations among the three simulations can be noted. However, they differ from each other by less than 1 %. Experimentally, from holographic interferograms, reattachment is estimated to occur at 1.6 ± 0.1 step heights from the step face or $s/h = 2.6 \pm 0.1$. (Hayne 2004). Thus, in general, in the reattachment region, all the simulations essentially yield the same results and chemical and thermal non-equilibrium effects are minimal.

https://doi.org/10.1017/jfm.2012.29 Published online by Cambridge University Press

Model	Separation s/h	Reattachment s/h
Perfect gas	0.0759	2.533
Chemical non-equilibrium	0.0759	2.512
Chemical plus thermal non-equilibrium	0.0755	2.584

TABLE 5. Normalised separation and reattachment distances for suborbital flow.

An important feature to note from both the Stanton number (figure 7) and skin friction (figure 8) distributions is that they all go to zero at the bottom corner of the step. This is a characteristic feature of a two-dimensional laminar flow at a concave corner, as pointed out by Jackson *et al.* (2001).

The pressure distributions in figure 8 indicate a relatively constant pressure upstream of the corner (see the inset) and, as the corner is approached, there is a continuous fall from the top corner, reaching a minimum on the face of the step at $s/h \approx 0.038$ as a result of over-expansion at the corner. Of particular note is the decrease in pressure on the forebody which begins at $s/h \approx -0.25$ which is the same as the location at which the skin friction and heat flux start to increase. The favourable pressure gradient allows for this rise in skin friction. With regard to the Goldstein singularity mentioned earlier, some comments are in order. While strictly the Goldstein singularity implies flow of $Re_L \to \infty$, in the present low-Reynolds-number flow, both skin friction and heat flux would be finite and grid converged. This is also reinforced by the fact that the corresponding pressure fall at the lip is also gradual and not discontinuous. It is, therefore, possible that gradients of the flow near the lip are smoothed by the strong viscous nature of the flow at the corner location. Nevertheless, it is interesting to note that steep gradients in heat flux and skin friction exist even in such low-Reynolds-number flows.

After $s/h \approx 0.038$, a steep recovery occurs as the flow is recompressed through a lip shock (Hama 1968). Subsequently, after $s/h \approx 0.2$, the pressure plateau is consistent with the constant pressure in the recirculation region that extends up to $s/h \approx 1.5$. Further increase in pressure is due to the reattachment process. An interesting feature to note from the pressure distributions and skin friction shown in figure 8 is that there is a small lag between the pressure minimum and the separation point at which the skin friction becomes zero. In his investigation of hypersonic laminar wakes of blunt bodies, such as cylinders, Dewey (1965) notes that the pressure minima occur at or very close to the separation point. As theorised by Weinbaum (1968), this is due to the fact that the singular nature of the sharp corner while allowing a sharp drop in pressure (due to the basically inviscid nature of the expansion), maintains finite shear which continues before eventually going to zero. This lag, therefore, is essentially due to the viscous nature of the flow around the corner that is accelerated in high-Mach-number and low-Reynolds-number flow. It should be noted that the above computational results could not be compared with any experimental data as no such data with sufficient resolution are available for a 2 mm step.

4.2. *Comparison with experiments*

It is widely appreciated, in hypervelocity aerothermodynamics especially (Harvey, Holden & Wadhams 2001), that both experiment and CFD must go hand in hand. In many an instance, the CFD can be very useful in probing regions of the flow

https://doi.org/10.1017/jfm.2012.29 Published online by Cambridge University Press

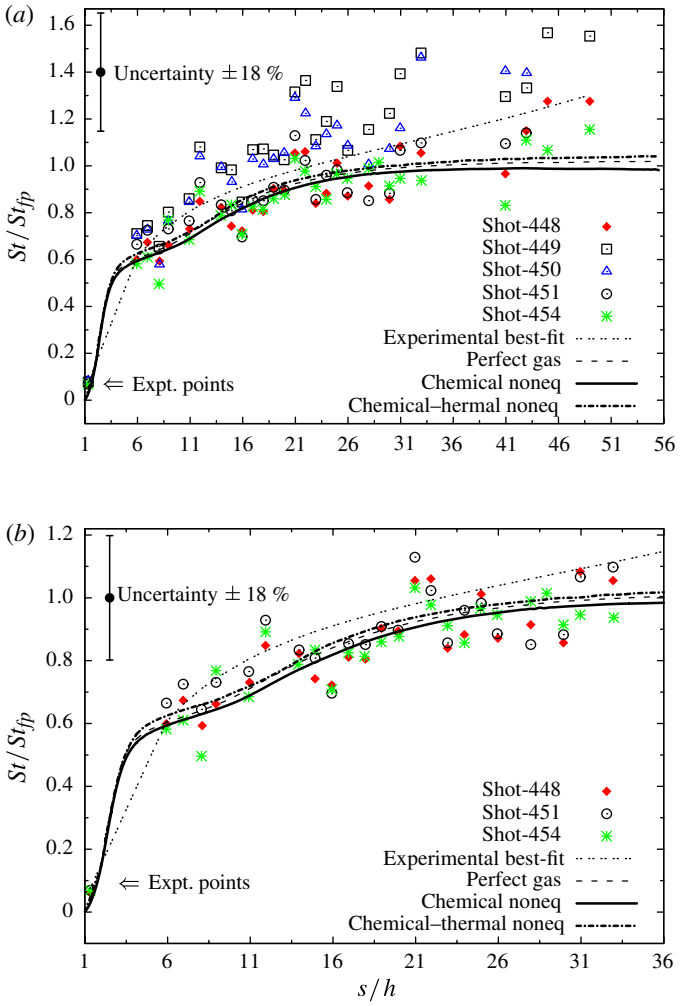


FIGURE 9. (Colour online) Experimental comparison of results downstream of the step in suborbital flow, $H_o = 26$ MJ kg^{-1}: (*a*) distributions between $1 \leqslant s/h \leqslant 56$; (*b*) distributions between $1 \leqslant s/h \leqslant 36$.

and to discern various fluid properties that are not easily accessible or amenable to experimental measurements. On the other hand, the experiments should also aim to provide reliable data to facilitate code development and evaluation. It is in this context that the comparison of numerical simulations and experimental data are made and discussed in this subsection and § 5.2.

Figure 9 shows the computations of heat flux, in terms of the normalised Stanton number (St/St_fp) compared with the experimental data of Hayne (2004) downstream of the step ($s/h \geqslant 1$). The Stanton number distributions downstream of the step (St) are normalised with the corresponding attached flat-plate Stanton number (St_fp) data for both the experimental and computational results. The flat-plate Stanton number computations are obtained by using the Grid-5 domain presented in figure 5, but excluding the blocks representing the step portion while retaining the cold wall boundary condition for the flat plate. This way, an exact cell-to-cell match between

https://doi.org/10.1017/jfm.2012.29 Published online by Cambridge University Press

the step and flat-plate computational domains, both upstream and downstream of the corner, is achieved.

Experimentally, five shots are considered at the same flow conditions and details of shot to shot variations are found in Hayne (2004). Using these data, an experimental best-fit curve is constructed. The normalised Stanton number distributions of the experimental shots, along with the best fit, are also shown in figure 9.

In figure 9(*a*), the computations corresponding to the perfect gas, chemical non-equilibrium and chemical plus thermal non-equilibrium are shown for $1 \leqslant s/h \leqslant 56$. It is seen that the computations show good agreement with the experiments up to about $s/h \leqslant 30$. The chemical non-equilibrium and chemical plus thermal non-equilibrium data do not deviate much from those of a perfect-gas and possible reasons for this are discussed below. Other features to note in figure 9(*a*) are that the computations deviate considerably from the experiments beyond $s/h \geqslant 30$, where they noticeably under-predict the normalised Stanton number values from shots 449 and 450. Also, figure 9(*a*) shows that, beyond $s/h \geqslant 30$, the experimental data exhibit a large scatter. It is very likely that, in the experiments, the flow is not fully established in this region, as has been demonstrated in Deepak (2010), and that a longer test time is generally required than was experimentally available.

In order to examine the comparisons within the region $1 \leqslant s/h \leqslant 30$ more clearly, computations along with experimental data from shots 448, 451 and 454, are re-plotted in figure 9(*b*). It is quite evident that the computations generally show better agreement considering that the experimental uncertainty is $\pm 18\,\%$. Experimental data in the region $2 \leqslant s/h \leqslant 6$ are sparse and, therefore, no clear comparison can be made. However, the computations do predict very well the nearest experimental data point at $s/h = 1.3$ immediately past the step. Both computations and experiments show heat flux approaching zero at the lower corner of the step. As noted earlier, this is a characteristic of two-dimensional laminar flow at a concave corner. Computations show a distinct plateau region between $3 \leqslant s/h \leqslant 11$. This is the result of the slipstream emanating due to the coalescence of the lip and recompression shocks. This feature is particularly evident in high-Mach-number and low-Reynolds-number separation and reattachment (Hama 1966). The experiments, however, do not give an indication of a plateau due to their large scatter.

Tchuen & Zeitoun (2009) recently compared their finite-rate chemistry simulations with some of the available experiments in high-Mach-number flows over blunt bodies. They provide detailed comparisons of various finite-rate chemistry models and the influence of reaction rates which includes the Park (1993) chemical plus thermal non-equilibrium model. Over a wide range of Mach numbers, they found that the Park (1993) kinetic scheme reasonably well predicts the effects of chemistry in hypersonic flows and closely matched the experimental data. This lends some confidence in the thermal plus chemical non-equilibrium heat flux data obtained here using the Park (1993) model.

4.3. *Effect of chemical reactions*

Hayne *et al.* (2004) estimated the surface and gas-phase Damköhler numbers for their experiments in the X2 expansion tube and suggested that the boundary layer was chemically frozen. A similar conclusion was arrived at by Gai *et al.* (1989) for the dissociated flow of air over a 3 and 6 mm step configuration at a specific total enthalpy of 19.8 MJ kg^{-1}. Gai *et al.* (1989) further suggest that the boundary layer upstream of separation and the separated shear layer remains chemically frozen with no effect of surface catalysis. Nevertheless, Hayne *et al.* (2004) indicate that there

https://doi.org/10.1017/jfm.2012.29 Published online by Cambridge University Press

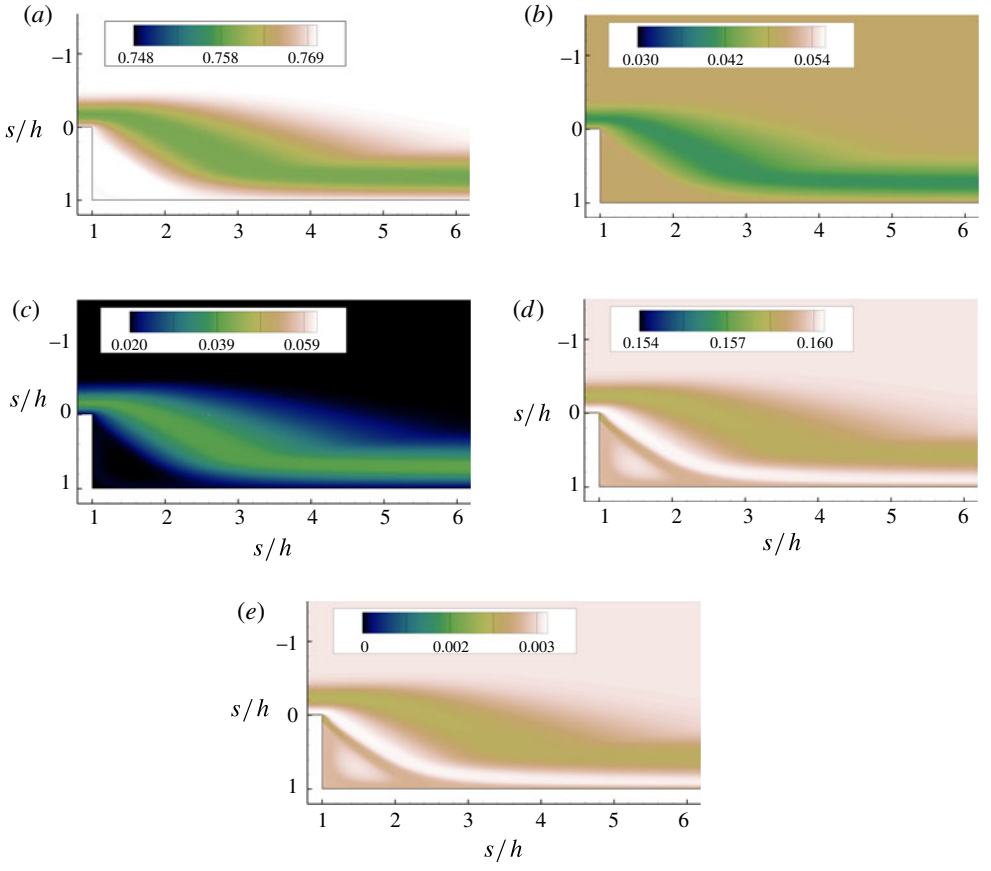


FIGURE 10. (Colour online) Contour map of species mass fractions behind the step in suborbital flow, $H_o = 26$ MJ kg^{-1}. Gupta *et al.* (1990): (*a*) N_2; (*b*) O_2; (*c*) NO; (*d*) O; (*e*) N.

could be some catalytic effects, although their influence is negligible for the surface heat transfer. Based on this assumption, the wall in the present study is treated as non-catalytic.

From the experiments it has been concluded that the flow is chemically frozen, especially downstream of the step where heat flux measurements were made. Also, our computations have showed that the effects of chemical reactions are not significant in the separated region. Nevertheless, detailed comparisons of the species concentration in the vicinity of the step are made, including downstream of reattachment over the plate.

In figures 10 and 11, contour maps of species concentrations immediately behind the step in the separation and reattachment region are shown for the Gupta *et al.* (1990) and Park (1993) reaction schemes respectively. Some dissociation of N_2 is seen upstream of the corner before separation (figure 10*a*); however, its extent is quite small and is nearly frozen and this is similar in both reaction schemes. After the flow separates, there is not much change in its concentration and it remains frozen even after reattachment. However, in the recirculation region, the concentration seems to be the same as that of the free stream. The peak temperature attained is not sufficient for any appreciable amount of N_2 dissociation.

https://doi.org/10.1017/jfm.2012.29 Published online by Cambridge University Press

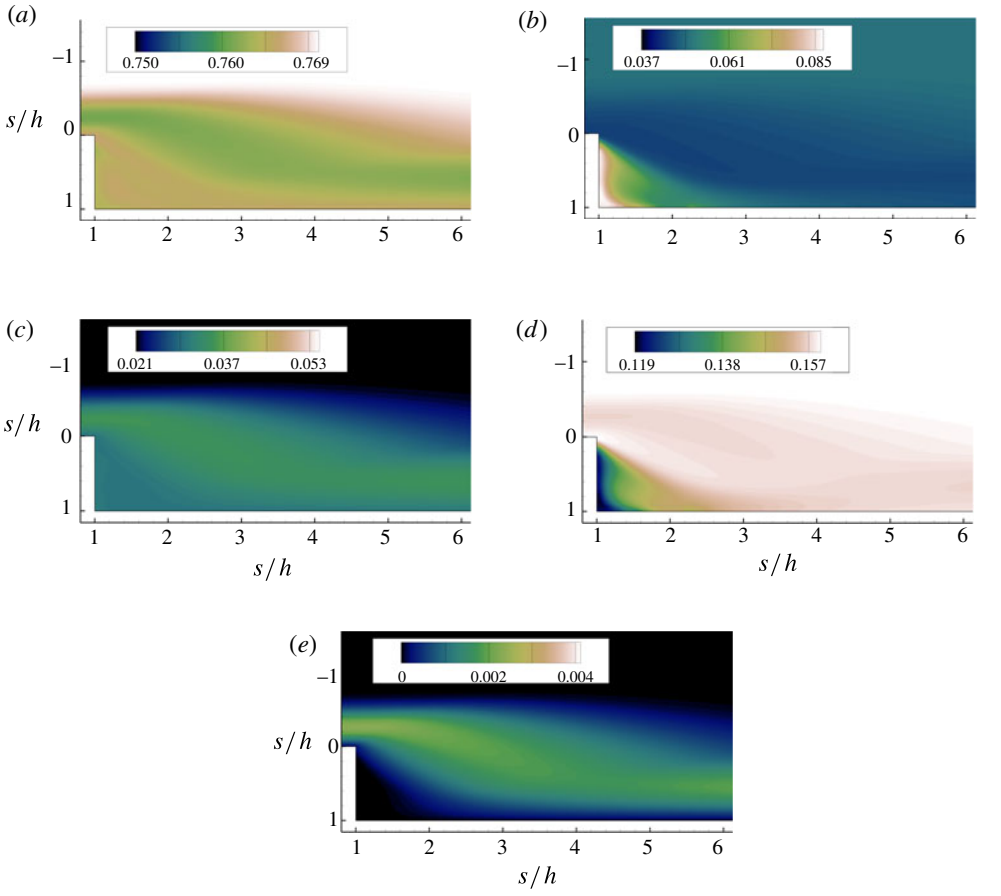


FIGURE 11. (Colour online) Contour map of species mass fractions behind the step in suborbital flow, $H_o = 26$ MJ kg^{-1}. Park (1993): (*a*) N_2; (*b*) O_2; (*c*) NO; (*d*) O; (*e*) N.

The O_2 mass fraction in figure 10(*b*), shows that most of it is already dissociated, having a maximum concentration of $X_{O_2} = 0.05$, as a result of the high free-stream temperature ($T_\infty \approx 1800$ K). Some of the remaining O_2 further dissociates in the viscous boundary and shear layers. Upon separation, it remains nearly frozen in the shear layer and does not undergo any further dissociation in the recirculation region. In contrast, for the Park (1993) scheme (figure 11*b*), a relatively higher concentration of O_2 can be seen in the recirculation region, particularly over the step face, and is consistent with the relatively lower concentration of O seen in figure 11(*d*). It would seem that there is some recombination occurring with atomic O, as a sufficiently longer residence time is achieved in the subsonic recirculation region. Such a possibility has also been suggested by Hayne *et al.* (2004). However, considering the time taken to achieve a steady separated flow, which is of the order of 100 μs, it may be too short for any exothermic recombination to occur and thus, does not have any appreciable effect on the heat flux, as seen from figure 7, except for a minimal rise. Downstream of reattachment, it can be seen that the O recovers to the free-stream concentration and then remains frozen in the Park (1993) scheme whereas, in the Gupta *et al.* (1990) scheme, such variations of either O_2 or O are not apparent, except that they are in the frozen state.

https://doi.org/10.1017/jfm.2012.29 Published online by Cambridge University Press

Concerning the endothermic formation of NO in figure 10(*c*), small amounts are formed upstream of the corner. After separation and downstream of reattachment, the trend appears to be the same and, within the recirculation region, a near free-stream concentration exists. In the Park (1993) scheme, the concentration of NO, as shown in figure 11(*c*), is relatively lower upstream of the corner, while in the recirculation region a moderately higher concentration than the Gupta *et al.* (1990) scheme seems to exist. It also appears nearly frozen within the recirculation region and downstream of reattachment.

In figure 10(*e*), the variation in atomic N is shown for the Gupta *et al.* (1990) scheme. Although its formation is evident upstream of the corner consistent with the dissociation of N_2, the concentrations are smaller. Similar behaviour is also seen in the Park (1993) scheme in figure 11(*e*). We also note that the extent of N_2 dissociation and the formation of N are moderately higher in the Gupta *et al.* (1990) scheme. However, under the influence of strong expansion at the corner, N is almost frozen in both schemes and appears to be so downstream of reattachment as well.

An important feature to note in figures 10 and 11 is that the flow is chemically frozen along the boundary layer over the forebody upstream of the corner. However, it is evident that across the boundary layer, reactions do occur. As the flow approaches the top corner and undergoes expansion, most of the reacted species in the separated shear layer tend to approach a chemically frozen state. This typically occurs because of the rapid decrease in density and pressure such that sufficient collisions between the species to reach equilibrium conditions do not occur. It takes a long distance downstream for the equilibrium conditions to exist. The influence of the vibrational temperature will be discussed in a later section of the paper.

5. Results and discussion: superorbital flow

5.1. *The vicinity of the step*

In this section, the flow features in the vicinity of the top corner of the step and between separation/reattachment are considered at superorbital conditions. The conditions for superorbital flow are among the highest, with a specific total enthalpy of $H_o \approx 50$ MJ kg^{-1}. Similar to the results of suborbital flow, the Stanton number, skin friction and pressure distributions are presented.

Figure 12 shows the Stanton number distributions. While the figure in general illustrates the flow between separation and reattachment, the inset emphasises the flow at the lip of the corner. We note that the perfect gas and the two real gas results exhibit the same trends as in suborbital flow. Characteristic features such as the asymptotic rise in heat flux at the separation discontinuity (top corner), the heat flux going to zero at the bottom corner and its monotonic recovery in the recirculation region and beyond are noted. As in suborbital flow, the recirculation region between separation and reattachment is mainly dominated by cold recirculating flow, in which no chemical reactions occur. Therefore, the influence of the real gas effects on the heat flux within this region is not very strong.

Figure 13 shows the corresponding results for the skin friction and pressure. Although, in general, the results are similar to those in suborbital flow, some interesting differences are evident. Firstly, over the forebody region, it is seen that the skin friction data from the three computations differ, but the difference between the two real gas models is not very large. The second feature is that the upstream influence is felt much further because of the thicker boundary layer at separation in view of the lower Reynolds number of the flow.

https://doi.org/10.1017/jfm.2012.29 Published online by Cambridge University Press

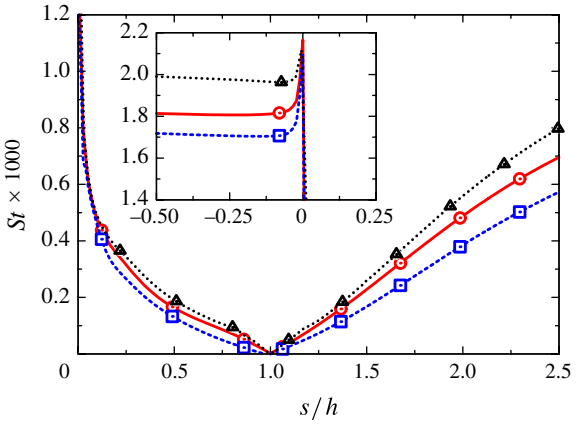


FIGURE 12. (Colour online) Stanton number distributions in the vicinity of the corner (inset) and between separation and reattachment in superorbital flow, $H_o = 50$ MJ kg^{-1}: $-\odot-$, perfect gas; $--\boxdot--$, chemical non-equilibrium; $--\triangle--$, chemical-thermal non-equilibrium.

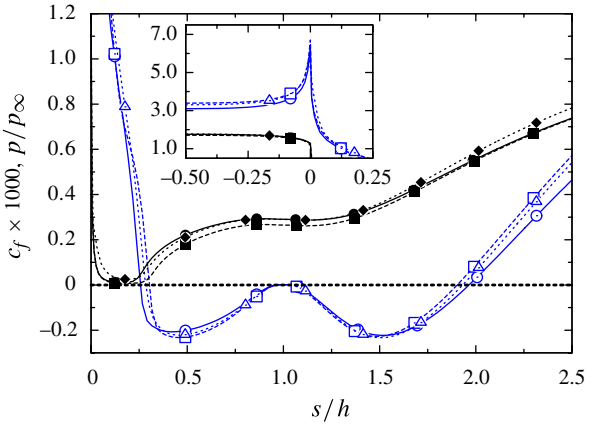


FIGURE 13. (Colour online) Skin friction coefficient and pressure distribution in the vicinity of the corner (inset) and between $-1.0 \leqslant s/h \leqslant 2.5$ in superorbital flow, $H_o = 50$ MJ kg^{-1}; ($c_f \times 1000$: $-\odot-$, perfect gas; $--\boxdot--$, chemical non-equilibrium; $\cdots\triangle\cdots$, chemical-thermal non-equilibrium); (p/p_∞: $-\bullet-$, perfect gas; $--\blacksquare--$, chemical non-equilibrium; $\cdots\blacklozenge\cdots$, chemical-thermal non-equilibrium).

From figure 13, it is seen that small differences exist among the three models in delineating separation and reattachment with perfect gas predicting the earliest separation and the chemical non-equilibrium predicting the furthest separation on the step face. We note that the pressure minimum is somewhat 'shallow' so that there does not appear to be a distinct minimum. A similar state of affairs is also noted when the skin friction goes to zero at the bottom corner ($s/h = 1$). These features illustrate the highly viscous nature of the flow at the step face. The differences among the three models at reattachment are smaller in comparison. The locations of separation and reattachment are given in table 6. It is seen that while the separation location differs by up to 16 % among the three models, the reattachment location

https://doi.org/10.1017/jfm.2012.29 Published online by Cambridge University Press

Model	Separation s/h	Reattachment s/h
Perfect gas	0.254	1.954
Chemical non-equilibrium	0.303	1.897
Chemical plus thermal non-equilibrium	0.291	1.924

TABLE 6. Normalised separation and reattachment distances for the superorbital flow.

varies by no more than 3 %. Between the two real gas models the differences between separation and reattachment are no more than 4 % and 1.5 % respectively. While the holographic interferometry was able to locate the reattachment in suborbital flow, this was not possible at superorbital flow condition due to very low pressures and densities in the separated region (Hayne 2004). An experimental verification was, therefore, not possible. What is important to notice, however, is that in superorbital flow the separation region is reduced by about a third compared to the suborbital flow. The superorbital flow is characterised by a lower Reynolds number where viscous effects are quite strong. This has a significant effect on the separation/reattachment mechanism as discussed earlier.

5.2. *Comparison with experiments*

Figure 14 compares the present computations with the experimental data obtained by Hayne (2004). As with the suborbital flow, there is again a considerable scatter in the experimental data and this fact has to be borne in mind while drawing any inference. Both the perfect gas and the chemical plus thermal non-equilibrium simulations are quite close to the experimental values while the chemical non-equilibrium simulation predicts the lowest heat flux. Figure 14(*b*) shows comparison with two shots 437 and 438, which have comparatively less scatter. This figure shows that the perfect gas and chemical plus thermal non-equilibrium simulations have reasonably good agreement with experiments up to $s/h \approx 36$. Close to the step, $1 \leqslant s/h \leqslant 8$, all the three simulations agree reasonably well with experimental data. Given that there are hardly any experimental data at such high enthalpies and given that there is some uncertainty in the establishment of steady test times in the experiments, the agreement achieved is quite reasonable and as far as the authors are aware, no such comparison between computational and experimental results currently exists. The distinct dip seen in suborbital flow is much less evident here although one can discern a shallow region between $8 \leqslant s/h \leqslant 31$. Again, this is the effect of highly viscous-dominated flow in which the lip shock seems to be embedded in the shear layer and the slipstream effect less perceptible, as will be shown later.

5.3. *Effect of chemical reactions*

Similar to the suborbital flow, the flow downstream of the step in the case of superorbital flow appears to be chemically frozen (Hayne 2004). In figures 15 and 16, contour maps of species concentrations in the vicinity of the corner and downstream of reattachment are presented for the Gupta *et al.* (1990) and Park (1993) schemes respectively. Here, the dissociation of N_2 is evident in the high-temperature region within the boundary layer upstream of separation and the amount of dissociation is relatively higher in the Gupta *et al.* (1990) model. With superorbital conditions, the peak temperature in the boundary layer is much higher so that some of N_2 dissociates.

https://doi.org/10.1017/jfm.2012.29 Published online by Cambridge University Press

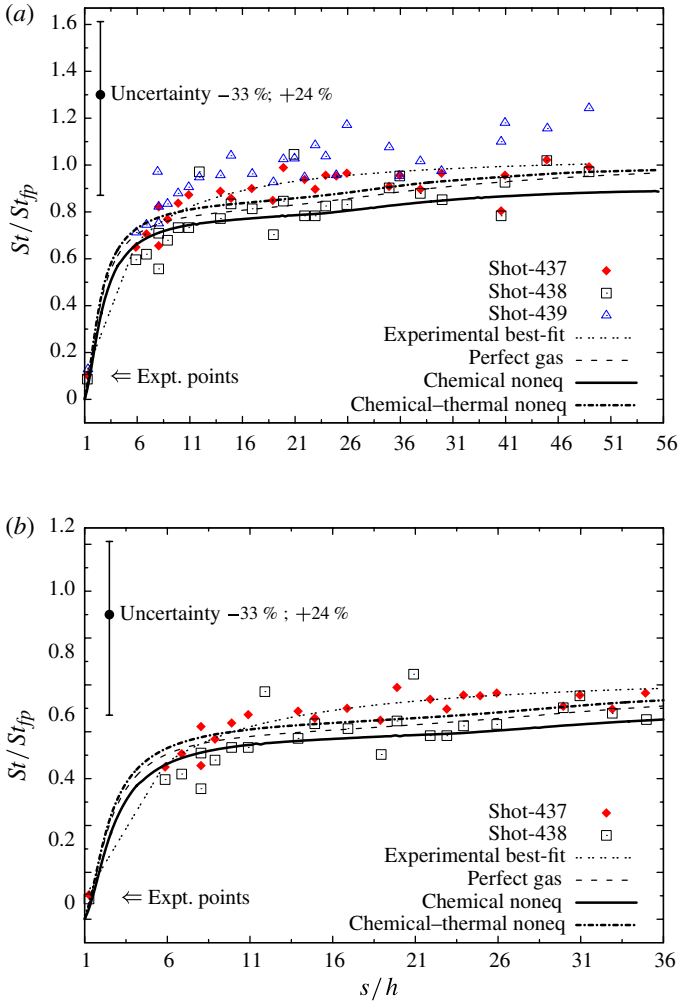


FIGURE 14. (Colour online) Experimental comparison of results downstream of the step in superorbital flow, $H_o = 50$ MJ kg^{-1}: (*a*) distributions between $1 \leqslant s/h \leqslant 56$; (*b*) distributions between $1 \leqslant s/h \leqslant 36$.

As the flow separates, the partially dissociated N_2 appears to be frozen in the shear layer and in the recirculation region. Downstream of reattachment, the dissociated N_2 in the shear layer remains frozen. This trend is consistent in both the reaction schemes.

Considering the concentration of O_2 in figure 15(*b*), it is fully dissociated in the free stream. However, small amounts of O_2 seem to form through the process of recombination which is consistent with the reduction in O in the same region (figure 15*d*). After separation, within the recirculation region, no such recombination is evident. In contrast, atomic oxygen recombines in the recirculation region forming O_2 in the Park (1993) scheme, as evident in figure 16(*b*) but seems confined to the bottom corner, possibly because of a small secondary vortex. Consequently, a small reduction in atomic O is seen (figure 16*d*). The recombination of oxygen atoms in the recirculation region was also noted with suborbital flow for the Park (1993) scheme; however, the mass fraction there seemed to be relatively higher.

https://doi.org/10.1017/jfm.2012.29 Published online by Cambridge University Press

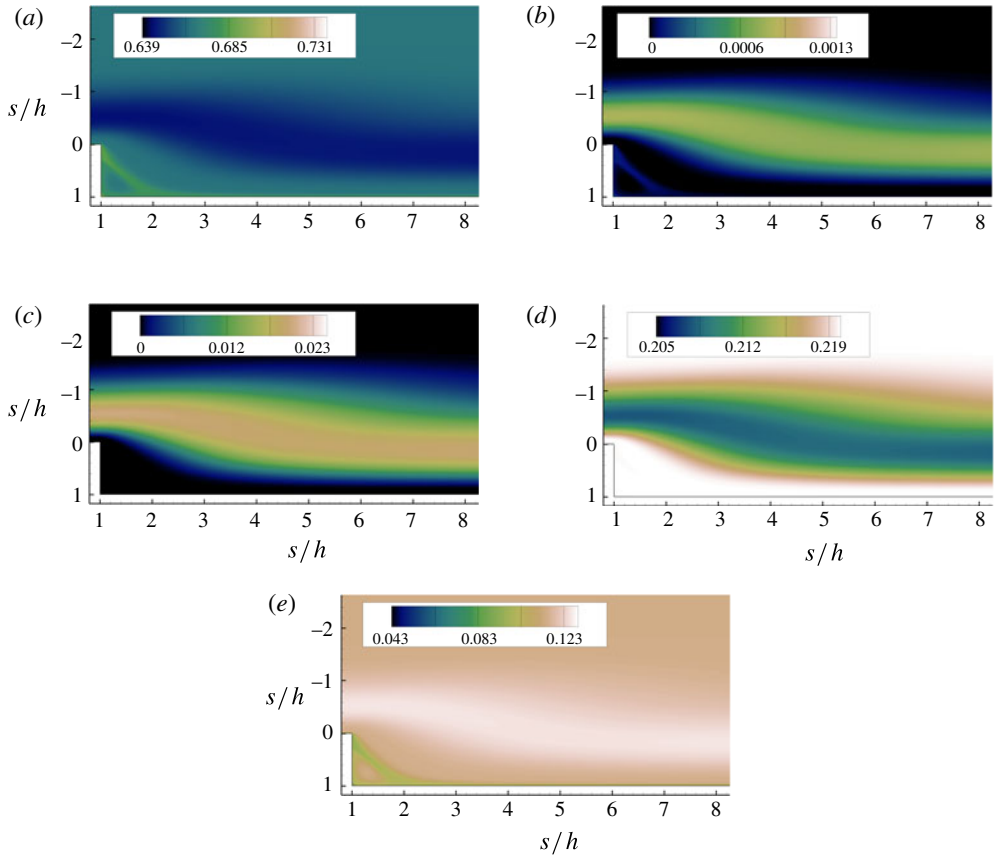


FIGURE 15. (Colour online) Contour map of species mass fractions behind the step in superorbital conditions, $H_o = 50$ MJ kg^{-1}. Gupta *et al.* (1990): (*a*) N_2; (*b*) O_2; (*c*) NO; (*d*) O; (*e*) N.

The formation of NO is evident with both reaction schemes, with higher concentrations predicted by the Gupta *et al.* (1990) scheme within the boundary layer and in the shear layer at separation and downstream of reattachment. Within the recirculation region, however, the concentrations are almost nil. The formation of atomic N can be seen in both schemes, being higher in the Gupta *et al.* (1990) scheme which is consistent with the degree of dissociation of N_2. Within the recirculation region, it is found that very small amounts of atomic N recombine to form N_2 close to the bottom corner. However, such an indication is not evident with the Gupta *et al.* (1990) scheme.

Several important features can be elucidated from figures 15 and 16. Firstly, the boundary layer upstream of the corner over the forebody region remains nearly frozen close to the wall, although reactions are evident in the high-temperature region of the boundary layer. As the flow approaches the corner and expands, the dissociated species in the separated shear layer are in a chemically frozen state. Within the recirculation region, and downstream of reattachment, the species continue to be in a frozen state, except that some minimal recombination is seen to occur in the recirculation region. Although these features were also noted with suborbital flow, the amounts of reactants here are different.

https://doi.org/10.1017/jfm.2012.29 Published online by Cambridge University Press

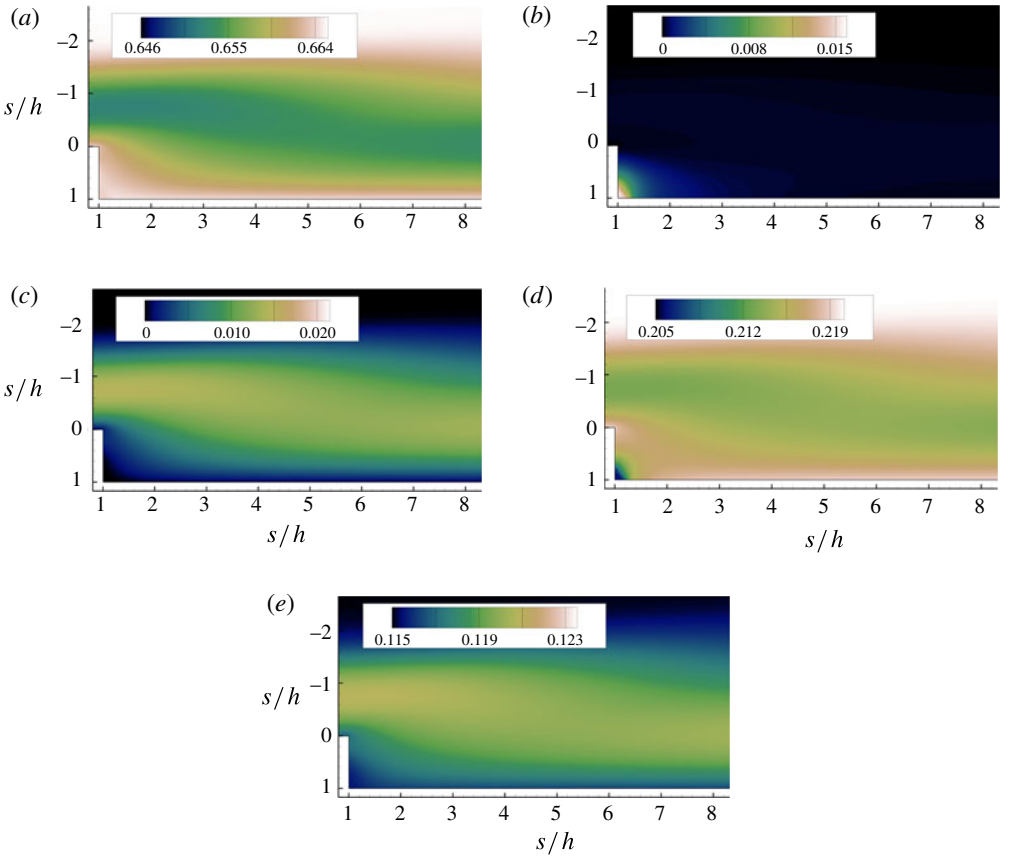


FIGURE 16. (Colour online) Contour map of species mass fractions behind the step for superorbital conditions, $H_o = 50$ MJ kg^{-1}. Park (1993): (*a*) N_2; (*b*) O_2; (*c*) NO; (*d*) O; (*e*) N.

6. Computational visualisation

In figure 17, the general features downstream of the step are shown through the Mach contours for both suborbital and superorbital flows. The boundary layer over the flat plate upstream of the corner can be clearly seen and, specifically, its relative thickness in comparison with the step height should be noted. In suborbital flow, the boundary layer thickness at separation is approximately 0.8 step heights, while in superorbital flow, it is nearly 2.5 step heights. Experimentally, from the interferogram images the boundary layer thickness was $\sim 0.9 \pm 0.1$ step heights for suborbital and 2.6 ± 0.2 step heights for superorbital flow. An expansion occurs at the corner followed by boundary layer separation. As can be seen, a thick separated shear layer forms as the flow turns round the corner giving rise to a recirculation region and reattachment. A recompression shock as a result of reattachment is also seen. The recompression shock is more clearly visible in suborbital flow as it emerges from within the shear layer while it appears to be completely embedded within the shear layer in superorbital flow. Since the boundary layer is thicker than the step height in superorbital flow, the shear layer downstream of reattachment is also very thick, as seen in figure 17(*b*).

https://doi.org/10.1017/jfm.2012.29 Published online by Cambridge University Press

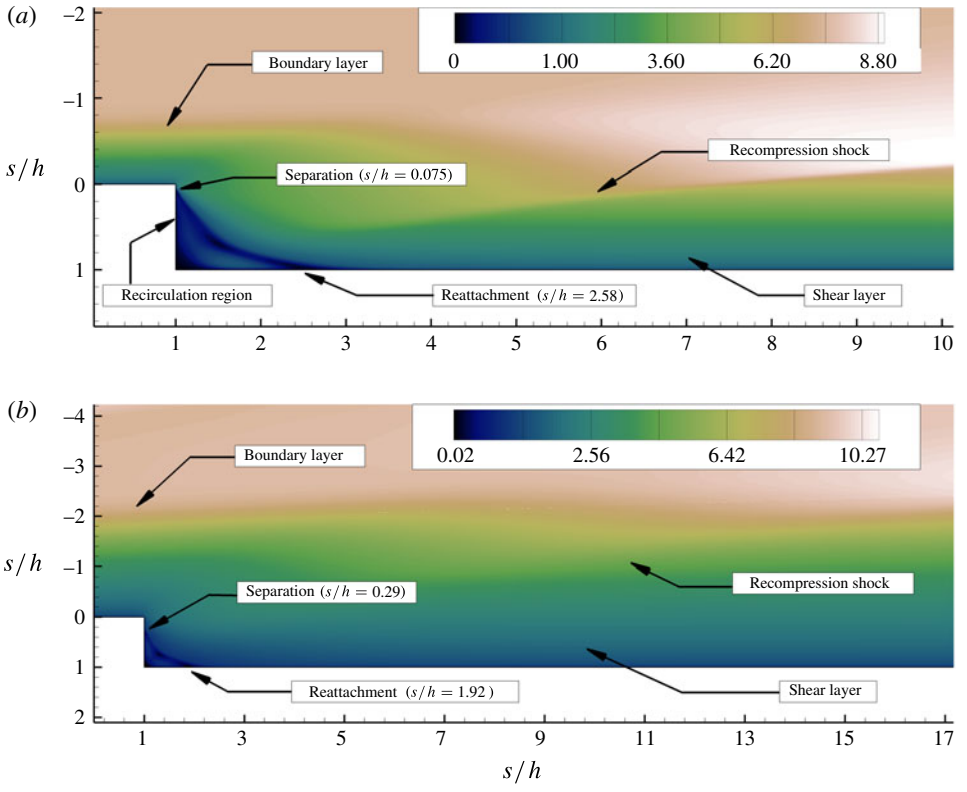


FIGURE 17. (Colour online) Close-up of Mach number contours behind the step: (*a*) suborbital flow, $H_o = 26$ MJ kg^{-1}; (*b*) superorbital flow, $H_o = 50$ MJ kg^{-1}.

Due to over-expansion of the flow around the top corner, and the combination of high Mach and low Reynolds numbers, the existence of a lip shock from within the shear layer can be inferred (Hama 1966, 1968). Although the lip shock is not clearly visible in figure 17 immediately downstream of the step, its existence will be verified through density contours discussed in the following paragraphs. Other features to note from the figure, are the separation just below the top corner and reattachment on the plate, and the subsonic recirculation region. A thick shear layer trails downstream and a boundary layer subsequent to reattachment seems to develop. Downstream of reattachment, the shear layer shows little curvature and is parallel for a long distance downstream which is also evident in the experimental results of Gai *et al.* (1989).

Due to the difficulty of visualising the lip shock in figure 17, magnitudes of the density gradient are shown in figure 18 in grey-scale. These magnitudes were obtained by computing

$$|\nabla\rho| = \sqrt{\rho_x^2 + \rho_y^2} \tag{6.1}$$

over the two-dimensional flow field, where ρ_x and ρ_y are the local density scalars in the x and y directions respectively. Formation of the lip shock is visible in figure 18(*a*) as is its coalescence with the reattachment shock within ~ 3 step heights in suborbital flow. In superorbital flow, the lip shock seems to have a strong curvature and its

https://doi.org/10.1017/jfm.2012.29 Published online by Cambridge University Press

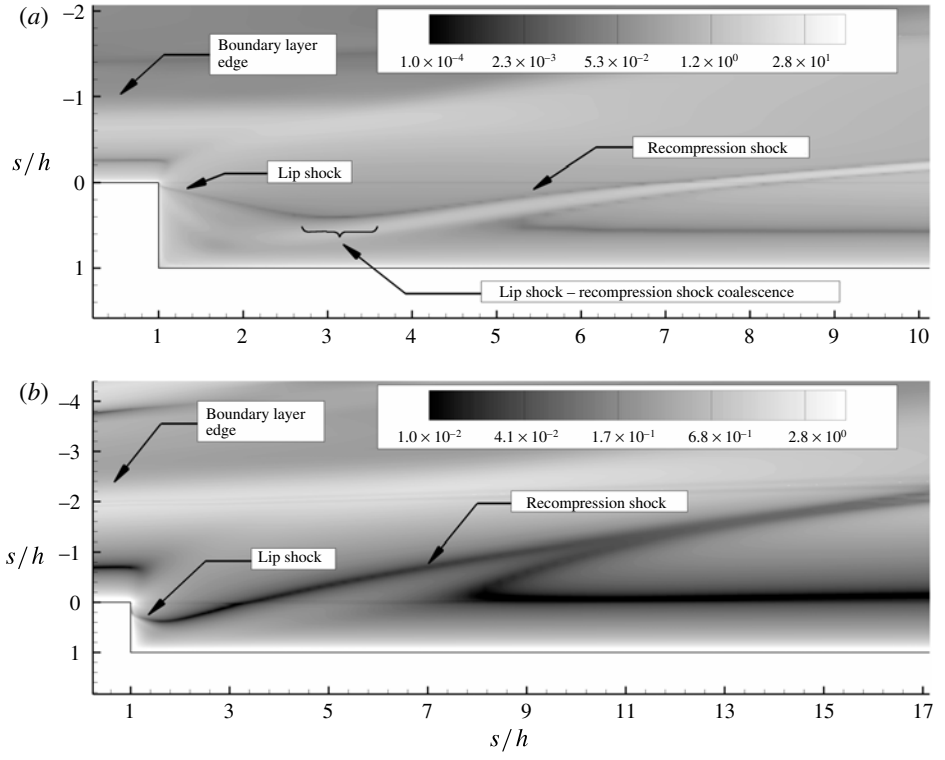


FIGURE 18. Density gradient $|\nabla\rho|$ contours behind the step: (*a*) suborbital flow, $H_o = 26$ MJ kg^{-1}; (*b*) superorbital flow, $H_o = 50$ MJ kg^{-1}.

coalescence seems to occur within a very short distance (figure 18*b*). This results in the recompression process being more gradual.

The streamlines computed using a commercial tool, Tecplot (2009) and superimposed on the normalised pressure contours are presented in figure 19 showing the influence of pressure on separation. The upstream influence on pressure is quite noticeable as the flow approaches the corner. In figure 19(*a*) for suborbital flow, the expansion can be seen to begin just upstream of the corner, whereas in superorbital flow (figure 19*b*), the upstream influence is much stronger and felt for a greater distance. Of further interest is the curvature of the expanding pressure waves. In suborbital flow, as the boundary layer is relatively thin, the expansion is relatively stronger and the Mach number gradient much steeper (figure 17) so that the curvature is quite large (Weinbaum 1966). In superorbital flow, with a very thick boundary layer, the curvature would be quite shallow.

Following the expansion around the corner, a recompression on the face of the step can be seen to occur which leads to separation due to the adverse pressure gradient on the face of the step. In the suborbital case, separation seems to occur at $s/h \approx 0.075$, while for the superorbital flow it is at $s/h \approx 0.3$. In both suborbital and superorbital flows, the base pressure is approached from below which is consistent with that postulated by Weinbaum (1968). It is interesting to note that both the recompression region and the base pressure are higher in superorbital flow. Again, as mentioned earlier this is due to the highly viscous nature of the flow round the corner and due to the fact that the lip shock and recompression shock

https://doi.org/10.1017/jfm.2012.29 Published online by Cambridge University Press

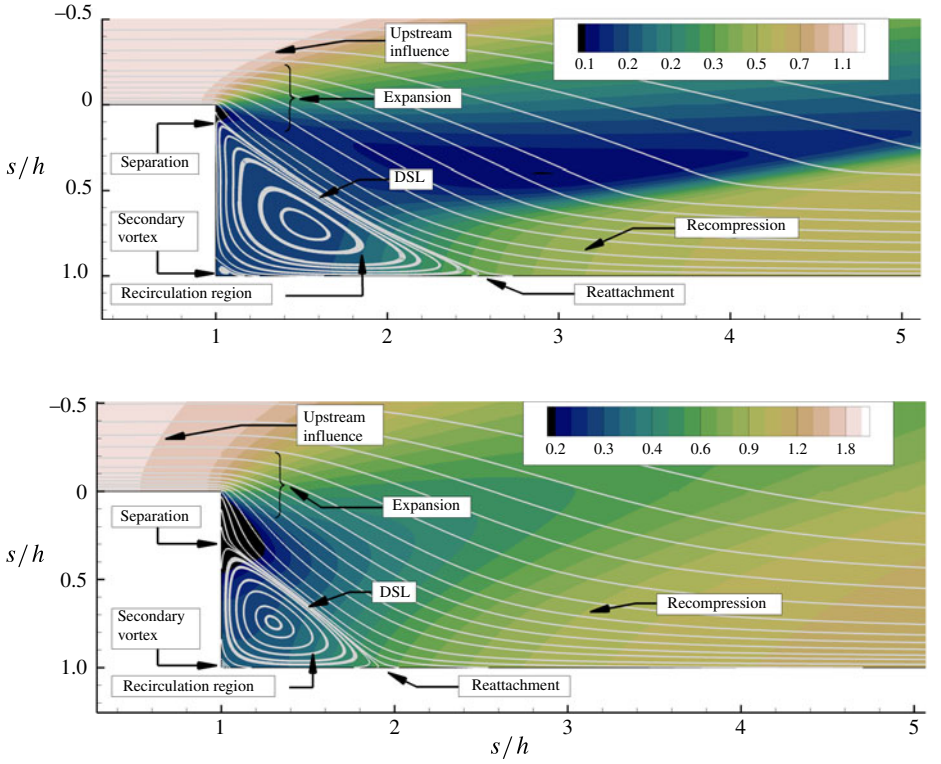


FIGURE 19. (Colour online) Computed streamlines over normalised pressure contours (p/p_∞) behind the step: (*a*) suborbital flow, $H_o = 26$ MJ kg^{-1}; (*b*) superorbital flow, $H_o = 50$ MJ kg^{-1}.

coalesce much closer to the base. As the streamlines reattach to the plate, the pressure increases and a recompression shock is formed. It should also be noted from the results of figures 18(*b*) and 19(*b*), that the consequence of the thick shear layer and the coalescence of the lip shock and the recompression shock both being embedded within the shear layer, is that the effect of slipstream is not strong.

In figure 20, ratios of the vibrational–electronic to translational–rotational temperatures (T_{v-e}/T_{t-r}) for both suborbital and superorbital flow are shown and they indicate the degree of thermal non-equilibrium in the flow. The thermal behaviour in the region upstream of the corner ($s/h \leqslant 1$) indicates an equilibrium flow in the inviscid region outside the boundary layer, where $T_{v-e}/T_{t-r} \approx 1$. Across the boundary layer, this ratio decreases, indicating thermal non-equilibrium even though the boundary layer itself is frozen. Within the boundary layer the peak heating zone can be seen where the translational temperature is much higher than the vibrational temperature. As the flow expands over the corner, T_{v-e} increases moderately but generally remains frozen. Within the recirculation region and, specifically, on the face of the step and up to $s/h \approx 2$ on the plate, $T_{v-e}/T_{t-r} \approx 1$ which suggests that the flow there is in thermal equilibrium. This is supported by the heat flux data in figures 7 and 12, where no great differences among the perfect gas, chemical non-equilibrium and chemical plus thermal non-equilibrium predictions are seen. Even after the shear

https://doi.org/10.1017/jfm.2012.29 Published online by Cambridge University Press

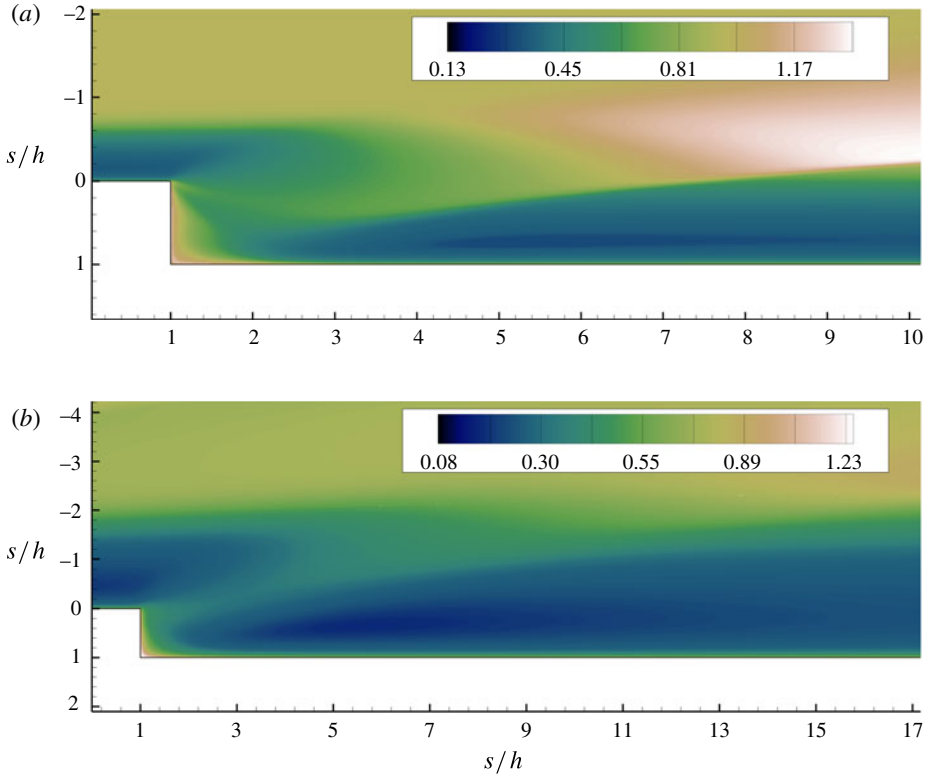


FIGURE 20. (Colour online) Contour map of the ratio of vibrational–electronic to translational–rotational temperature (T_{v-e}/T_{t-r}) behind the step: (*a*) suborbital flow, $H_o = 26$ MJ kg^{-1}; (*b*) superorbital flow, $H_o = 50$ MJ kg^{-1}.

layer reattaches, the flow remains in a thermally frozen state. Because of the smaller recirculation region in superorbital flow, the thermal equilibrium region is confined to the bottom corner.

Figure 21 shows a specific vorticity (ω/ρ) contour map superimposed on the streamlines in the separated region for both suborbital and superorbital flows. The vorticity contours were obtained with perfect gas simulations. The results with the two real gas simulations, namely chemical non-equilibrium and chemical plus thermal non-equilibrium, were qualitatively very similar. Any quantitative differences among the three simulations were not very significant which is not surprising as the real gas effects in the separation region are not strong.

7. Summary and conclusions

A computational investigation has been carried out for the flow over a rearward-facing step in high-enthalpy laminar hypersonic flow. The main focus was to analyse the separated flow under both suborbital and superorbital conditions and under the assumption of both perfect and real gas behaviour. Firstly, a detailed quantification of flow features in terms of various thermodynamic assumptions in the separation and reattachment regions was carried out. A detailed flow map of the highly viscous region of the flow around the separation lip, recirculation, and reattachment region is presented. The presence of a Goldstein-like singularity at the lip of the corner was

https://doi.org/10.1017/jfm.2012.29 Published online by Cambridge University Press

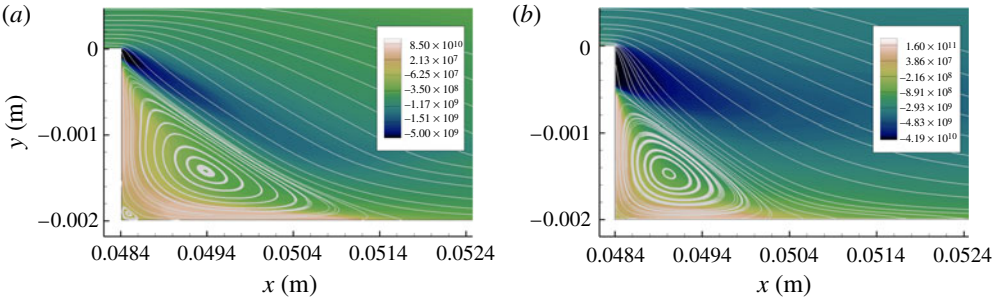


FIGURE 21. (Colour online) Contour map of specific vorticity (ω/ρ) behind the step; (*a*) suborbital flow, $H_o = 26$ MJ kg^{-1}; (*b*) superorbital flow, $H_o = 50$ MJ kg^{-1}.

evident and the pressure minimum occurred close to the location of separation on the step face. Recompression over the base of the step resulting in a lip shock then gave rise to the eventual base pressure.

In suborbital flow, the lip and recompression shock coalescence was clearly evident with the emergence of a slipstream while, in superorbital flow, the lip shock was seen to have a strong curvature and coalesced with the recompression shock within a very short distance from the step face, and was well embedded within the shear layer.

On the plate downstream of the step, the computations have been compared with the available experimental heat flux measurements. Reasonably good agreement was obtained for both suborbital and superorbital flows for up to ∼30 step heights. Further downstream, considerable differences between the computations and experimental data were noted and possible reasons for this are given.The chemical plus thermal non-equilibrium simulations seemed to yield results closest to the experimental values. The reasons for small differences observed among the three simulation models are also given. It should, however, be stated that in view of the large uncertainty in the experimental data, any differences between the three simulations are comparatively small but the simulations do show that the chemical and chemical plus thermal non-equilibrium data are close to each other, with the perfect gas data further away from them. These comparisons have emphasised the clear need for better experimental data to validate the computational simulations.

Both separation and reattachment locations were predicted reasonably well by all three simulations for both suborbital and superorbital flows. The reattachment location in suborbital flow could be confirmed by experimental evidence. Effects of real gas on separation and reattachment regions were found to be small.

The species mass fractions in the close vicinity of the step between the two reaction schemes (Gupta *et al.* 1990; Park 1993) have been analysed. Some presence of endothermic reactions was apparent within the boundary layer upstream of separation and in the shear layer after separation and downstream of reattachment. Within the recirculation region, some recombination was evident but it was too small to have any effect on the heat flux. The shear layer downstream of reattachment was also chemically frozen for both flow conditions, except that a very small amount of nitrogen atoms was evident. The influence of vibrational temperature was also studied and found to be predominantly frozen, especially in the expansion region immediately past the corner. Close to the step face and within the recirculation region, it was in equilibrium with the translational temperature. Downstream of reattachment, again, it was found that the flow was thermally frozen.

https://doi.org/10.1017/jfm.2012.29 Published online by Cambridge University Press

Acknowledgements

The authors would like to express their sincere thanks to Dr P. Jacobs of the University of Queensland for allowing us to use his MB-CNS-2 and Eilmer-3 solvers. Thanks are also due to Dr R. Gollan of NASA Langley Research Center for his support in explaining various intricacies in these solvers and their usability. We also wish to express our thanks to Professor R. Hillier of Imperial College, London for his valuable suggestions. We would also like to express our thanks to the referees for their comments and suggestions which have led to the improvement of the paper.

REFERENCES

AIAA, 1994 Policy statement on numerical accuracy and experimental uncertainty. *AIAA J.* **32** (1) 3 (editorial).

AIT-ALI-YAHIA, D. 1996 A finite element segregated method for thermo-chemical equilibrium and non-equilibrium hypersonic flows using adapted grids. PhD thesis, Concordia University.

VAN ALBADA, G. D., LEER, B. V. & ROBERTS, W. W. 1982 A comparative study of computational methods in cosmic gas dynamics. *Astron. Astrophys.* **108** (1), 76–84.

ALLEN, J. S. & CHENG, S. I. 1970 Numerical solution of the compressible Navier–Stokes equations for the laminar near wake. *Phys. Fluids* **13** (1), 37–51.

ANDERSON, W. K. & THOMAS, J. L. 1986 A comparison of finite volume flux vector splittings for the euler equations. *AIAA J.* **24** (9), 1453–1460.

BAKER, P. J. & MARTIN, W. 1966 Heat transfer in supersonic separated flow over a two-dimensional backward-facing step. *Intl J. Heat Mass Transfer* **9** (10), 1081–1088.

BERTIN, J. J. & CUMMINGS, R. M. 2003 Fifty years of hypersonics: where we've been, where we're going. *Prog. Aeronaut. Sci.* **39** (6–7), 511–536.

BERTIN, J. J. & CUMMINGS, R. M. 2006 Critical hypersonic aerothermodynamic phenomena. *Annu. Rev. Fluid Mech.* **38**, 129–157.

BOROVOI, V. YA, SKURATOV, A. K. & YEGOROV, L. V. 1998 Aerothermal study of martian probe. In *Proceedings of the Third European Symposium on Aerothermodynamics for Space Vehicles, 24–26th November 1998*, ESTEC, Noordwijk, The Netherlands, ESA SP-426.

CHEN, Y.-K., HENLINE, W. D., STEWART, D. A. & CANDLER, G. V. 1993 Navier–Stokes solutions with surface catalysis for martian atmospheric entry. *J. Spacecr. Rockets* **30** (1), 32–42.

CORDA, S. 1982 Numerical investigation of the laminar, supersonic flow over a rearward-facing step using an adaptive grid scheme. Master's thesis, Department of Aerospace Eningeering, University of Maryland.

DEEPAK, N. R. 2010 Computational studies of hypersonic high enthalpy separated flows. PhD thesis, School of Engineering and Information Technology, University of New South Wales, Australian Defence Force Academy.

DEEPAK, N. R., GAI, S. L. & NEELY, A. J. 2010*a* A computational study of high enthalpy flow over a rearward facing step. In *48th AIAA Aerospace Sciences Meeting Including the New Horizons Forum and Aerospace Exposition in Orlando, Florida, 4–7 Jan. 2010. AIAA* 2010-444.

DEEPAK, N. R., GAI, S. L. & NEELY, A. J. 2010*b* Investigation of heat-flux in high enthalpy hypersonic flow over a rearward-facing step. *Intl J. Hypersonics* **1** (2), 115–134.

DEWEY, C. F. 1965 A correlation of convective heat transfer and recovery temperature data for cylinders in compressible flow. *Intl J. Heat Mass Transfer* **8**, 245–252.

DONALDSON, I. S. 1967 On the separation of a supersonic flow at a sharp corner. *AIAA J.* **5** (6), 1086–1088.

DRUGUET, M.-C., BEN-DOR, G. & ZEITOUN, D. 2007 The interaction of supersonic and hypersonic flows with a double cone: comparison between inviscid, viscous, perfect and real gas model simulations. In *26th International Symposium on Shock Waves, Gottingen, Germany*, vol. 2.

https://doi.org/10.1017/jfm.2012.29 Published online by Cambridge University Press

DRUGUET, M.-C., CANDLER, G. V. & NOMPELIS, I. 2005 Effects of numerics on Navier–Stokes computations of hypersonic double-cone flows. *AIAA J.* **43** (3), 616–623.

GAI, S. L. 1992 Separated high enthalpy dissociated laminar hypersonic flow behind a step-pressure measurements. *AIAA J.* **30** (7), 1915–1918.

GAI, S. L., HAYNE, M. J., GARDNER, A. D., MORGAN, R. G. & MEE, D. J. 2001 Heat transfer behind a step in high enthalpy super-orbital flow. In *Proceedings of the 39th Aerospace Sciences Meeting and Exhibit, 8–11 Jan. 2001, Reno, Nevada. AIAA* 2001-509.

GAI, S. L. & MILTHORPE, J. F 1995 Hypersonic high-enthalpy flow over a blunt-stepped cone. In *20th International Symposium on Shock Waves, Pasadena, California, 23–28 July 1995*.

GAI, S. L., REYNOLDS, N. T., ROSS, C. & BAIRD, J. P. 1989 Measurements of heat transfer in separated high-enthalpy dissociated laminar hypersonic flow behind a step. *J. Fluid Mech.* **199**, 541–561.

GNOFFO, P. A. 2001 CFD validation studies for hypersonic flow prediction. In *39th AIAA Aerospace Sciences Meeting & Exhibit, 8–11 Jan. 2001*, Reno, Nevada. *AIAA* 2001-1025.

GOLDSTEIN, S. 1946 On laminar boundary-layer flow near a position of separation. *Q. J. Mech. Appl. Maths* **1**, 43–69.

GOLLAN, R. J. 2008 The computational modelling of high-temperature gas effects with application to hypersonic flows. PhD thesis, Department of Mechanical Engineering, University of Queensland.

GORDON, S. & MCBRIDE, B. J. 1994 Computer program for calculation of complex chemical equilibrium compositions and applications. I. Analysis. *NASA Tech. Rep.*, Reference Publication 1311.

GORSHKOV, A. B. & LUNEV, V. V. 2002 Laminar base flow downstream of slender cones in hypersonic flow. *Fluid Dyn.* **37** (5), 772–783.

GRASSO, F. & PETTINELLI, C. 1995 Analysis of laminar near-wake hypersonic flows. *J. Spacecr. Rockets* **32** (6), 970–980.

GROTOWSKY, I. M. G. & BALLMANN, J. 2000 Numerical investigation of hypersonic step-flows. *Shock Waves* **10** (1), 57–72.

GUPTA, R. N., YOS, J. M., THOMPSON, R. A. & LEE, K.-P. 1990 A review of reaction rates and thermodynamic and transport properties for an 11-species air model for chemical and thermal non-equilibrium calculations to 30000 K. *NASA Tech. Rep.* 1232.

HAMA, F. R. 1966 Experimental investigations of wedge base pressure and lip shock. *Tech. Rep.* N67 14905. Jet Propulsion Laboratory, California Institute of Technology, Pasadena, California.

HAMA, F. R. 1968 Experimental studies on the lip shock. *AIAA J.* **6** (2), 212–219.

HARVEY, J. K., HOLDEN, M. S. & WADHAMS, T. P. 2001 Code validation study of laminar shock/boundary layer and shock/shock interactions in hypersonic flow. Part b. Comparison with Navier–Stokes and DSMC solutions. In *Aerospace Sciences Meeting and Exhibit, 39th, Reno, Nevada, Jan. 8–11, 2001*.

HAYNE, M. J. 2004 Hypervelocity flow over rearward-facing steps. PhD thesis, Department of Mechanical Engineering, University of Queensland.

HAYNE, M. J., GAI, S. L., HILLIER, R., MORGAN, R. G., MEE, D. J. & MCINTYRE, T. J. 2002 Heat transfer and flow behind a rearward facing step in a super-orbital expansion tube. In *23rd International Symposium on Shock Waves, 22–27 July 2002* Fort Worth, Texas, USA (ed. F. K. Lu), pp. 1574–1580.

HAYNE, M. J., GAI, S. L., MEE, D. J. & MORGAN, R. G. 2004 Real gas effects on flows over rearward-facing steps. In *Proceedings of 24th International Symposium on Shock Waves, Beijing, China*, pp. 251–256.

HAYNE, M. J., MEE, D. J., MORGAN, R. G., GAI, S. L. & MCINTYRE, T. J. 2003 Heat transfer and flow behind a step in high enthalpy superorbital flow. *Aeronaut. J.* **107** (2778), 435–442.

HOLDEN, M. S. 1971 Establishment time of laminar separated flows. *AIAA J.* **9** (11), 2296–2298.

HOLLIS, B. R. & PERKINS, J. N. 1999 Transition effects on heating in the wake of a blunt body. *J. Spacecr. Rockets* **36** (5), 668–674.

JACKSON, A. P., HILLIER, R. & SOLTANI, S. 2001 Experimental and computational study of laminar cavity flows at hypersonic speeds. *J. Fluid Mech.* **427**, 329–358.

https://doi.org/10.1017/jfm.2012.29 Published online by Cambridge University Press

JACOBS, P. A. 1991 Single-block Navier–Stokes integrator. *Tech. Rep.* ICASE Interim Report 18. NASA Langley Research Center, Hampton, VA.

JACOBS, P. A. 1996 MB-CNS: a computer program for the simulation of transient compressible flows. *Tech. Rep.* 10/96. Department of Mechanical Engineering, University of Queensland.

JACOBS, P. A. & GOLLAN, R. J. 2010 The Eilmer3 code. *Tech. Rep.* 2008/07. Department of Mechanical Engineering, University of Queensland.

JACOBS, P. A., GOLLAN, R. J., DENMAN, A. F., O'FLAHERTY, B. T., POTTER, D. F., PETRIE-REPAR, P. J. & JOHNSTON, I. A. 2010 Eilmer's theory book: basic models for gas dynamics and thermochemistry. *Tech. Rep.* 2010/09. Department of Mechanical Engineering, University of Queensland, Brisbane.

JAKUBOWSKI, A. K. & LEWIS, C. H. 1974 Rearward-facing steps in laminar supersonic flows with and without suction. *NASA Tech. Rep.* NASA-CR-132476.

KHAN, O. U. & HOFFMANN, K. A. 2010 Unsteady supersonic flows over a backward-facing step with applied magnetic field. *J. Spacecr. Rockets* **47** (3), 405–412.

KURUVILA, G. & ANDERSON, J. D. 1985 A study of the effects of numerical dissipation on the calculation of supersonic separated flow. In *23rd AIAA Aerospace Sciences Meeting, January 14–17, 1985*, Reno, Nevada. *AIAA* 85-0301.

LEER, B. V. 1979 Towards the ultimate conservative difference scheme. V. A second-order sequel to Godunov's method. *J. Comput. Phys.* **32**, 101–136.

LEITE, P. H. M. & SANTOS, W. F. N. 2009 Direct simulation calculations of the rarefied hypersonic flow past a backward-facing step. In *3rd CTA-DLR Workshop on Data Analysis & Flight Control, Brazilian Symposium on Aerospace Engineering & Applications*.

MCBRIDE, B. J. & GORDON, S. 1996 Computer program for calculation of complex chemical equilibrium compositions and applications. II. User manual and program description. *NASA Tech. Rep. Reference Publ.* 1311.

MILLIKAN, R. C. & WHITE, D. R. 1963 Systematics of vibrational relaxation. *J. Chem. Phys.* **39** (12), 3209–3213.

MOTT, D. R. 1999 New quasi-steady-state and partial-equilibrium methods for integrating chemically reacting systems. PhD thesis, The University of Michigan.

PACIORRI, R., SABETTA, F. & FAVINI, B. 1998 On the role of vibrational excitation in hypersonic flow computations. *Meccanica* **33** (4), 331–347.

PAPADOPOULOS, P., VENKATAPATHY, E., PRABHU, D. & LOOMIS, M. P. 1999 Current grid-generation strategies and future requirements in hypersonic vehicle design, analysis and testing. *Appl. Math. Model.* **23** (9), 705–735.

PARK, C. 1993 Review of chemical-kinetic problems of future NASA missions. I. Earth entries. *J. Thermophys. Heat Transfer* **7** (3), 385–398.

PARK, G., GAI, S. L. & NEELY, A. J. 2010 Aerothermodynamics behind a blunt body at superorbital speeds. *AIAA J.* **48** (8), 1804–1816.

PRIOLO, F. J. 1983 The effect of grid compression on the accuracy of numerical solutions for laminar supersonic flow over a rearward facing step. Master's thesis, Department of Aerospace Eningeering, University of Maryland.

ROACHE, P. J. 1997 Quantification of uncertainty in computational fluid dynamics. *Annu. Rev. Fluid Mech.* **29**, 123–160.

ROACHE, P. J, GHIA, K. N. & WHITE, F. M. 1986 Editorial policy statement on the control of numerical accuracy. *Trans. ASME: J. Fluids Engng* **108**, 2.

ROACHE, P. J & MUELLER, T. J. 1968 Numerical solutions of compressible and incompressible laminar separated flows. In *AIAA Fluid and Plasma Dynamics Conference, Los Angeles, California, June 24–26, 1968. AIAA* 1968-741.

ROM, J. & SEGINER, A. 1964 Laminar heat transfer to a two-dimensional backward facing step from the high-enthalpy supersonic flow in the shock tube. *AIAA J.* **2** (2), 251–255.

ROSS, B. B. & CHENG, S. I. 1971 A numerical solution of the planar supersonic near-wake with its error analysis. In *Proceedings of the Second International Conference on Numerical Methods in Fluid Dynamics*, *Lecture Notes in Physics*, vol. 8/1971. pp. 164–169.

RUFFIN, S. M. & PARK, C. 1993 Vibrational relaxation of anharmonic oscillators in expanding flows. *J. Spacecr. Rockets* **30** (1), 59–68.

https://doi.org/10.1017/jfm.2012.29 Published online by Cambridge University Press

SANDFORD, J. & GINOUX, J. J. 1968 Laminar, transitional and turbulent heat transfer behind a backward facing step in supersonic flow. *Tech. Rep.* 38, Von Karman Institute for Fluid Dynamics.

SCHERBERG, M. G. & SMITH, H. E. 1967 An experimental study of supersonic flow over a rearward facing step. *AIAA J.* **5** (1), 51–56.

STEWARTSON, K. 1968 On the flow near the trailing edge of a flat plate. *Proc. R. Soc.* A **306** (1486), 275–290.

TCHUEN, G. & ZEITOUN, D. E. 2009 Effects of chemistry in non-equilibrium hypersonic flow around blunt bodies. *J. Thermophys. Heat Transfer* **23** (3), 433–442.

TECPLOT, 2009 Tecplot 360, 2009, Tecplot, Inc. (formerly Amtec Engineering, Inc.) 3535 Factoria Blvd S.E. Suite 550 Bellevue, WA 98006.

WADA, I. & INOUE, Y. 1973 Heat transfer behind a backward facing step. *Heat Transfer Japan. Res.* **2** (2), 39–42.

WADA, Y. & LIOU, M. S. 1994 A flux splitting scheme with high-resolution and robustness for discontinuities. In *Aerospace Sciences Meeting and Exhibit, 32nd, Reno, Nevada, Jan. 10–13*, 1994. *AIAA* 1994-83.

WEINBAUM, S. 1966 Specialist meeting on separated flows. In *AGARD Conference Proceedings 4*. Brussels.

WEINBAUM, S. 1968 On the singular points in the laminar two-dimensional near wake flow field. *J. Fluid Mech.* **33** (1), 39–63.

WILKE, C. R. 1950 A viscosity equation for gas mixtures. *J. Chem. Phys.* **18** (4), 517–519.

https://doi.org/10.1017/jfm.2012.29 Published online by Cambridge University Press